UC Berkeley
UC Berkeley Electronic Theses and Dissertations

Title
Graphene Growth on Low Carbon Solubility Metals

Permalink
https://escholarship.org/uc/item/3hs1q7q7

Author
Wofford, Joseph Monroe

Publication Date
2012

Peer reviewed|Thesis/dissertation

Graphene Growth on Low Carbon Solubility Metals

By

Joseph Monroe Wofford

A dissertation submitted in partial satisfaction
of the requirements for the degree of

Doctor of Philosophy

in

Engineering – Materials Science and Engineering

in the

Graduate Division

of the

University of California, Berkeley

Committee in charge:

Professor Oscar D. Dubón, Chair
Professor Andrew Minor
Professor Feng Wang

Spring 2012

Abstract

Graphene Growth on Low Carbon Solubility Metals

by

Joseph Monroe Wofford

Doctor of Philosophy in Engineering – Materials Science and Engineering

University of California, Berkeley

Professor Oscar D. Dubón, Chair

Advances in synthesis are imperative if graphene is to fulfill its scientific and technological potential. Single crystal graphene of is currently available only in the small flakes generated by mechanical exfoliation. Layers of larger size may be grown either by the thermal decomposition of SiC or by chemical vapor deposition on metals. However, as they are currently implemented, these methods yield graphene films of inferior quality. Thus the requirement for wafer-scale, high-quality graphene films remains unmet. This dissertation addresses this issue by examining graphene growth on metal surfaces. Through a survey of the fundamental underlying processes, it provides guidance for improving the quality of the resulting graphene films.

Graphene was grown on Cu(100), Cu(111), and Au(111) by physical vapor deposition of elemental C. The nucleation and growth behaviors of graphene were evaluated by low-energy electron microscopy. Graphene tends to nucleate heterogeneously at surface imperfections although it also does so homogeneously on Cu(111) and Au(111). Graphene growing on Cu(100) is governed by the attachment kinetics of C at the propagating crystal front. The resulting angularly dependent growth rate sculpts individual crystals into elongated lobes. In contrast, graphene growth on both Cu(111) and Au(111) is surface diffusion limited. This yields ramified, dendritic graphene islands.

Graphene films grown on Cu(100) contain significant rotational disorder. This disorder is partially attributable to the symmetry mismatch between film and substrate. The common symmetry between graphene and Cu(111) contributes to a significant reduction in disorder in films grown on this surface. Most graphene domains occupy a ~6° arc of orientations. On Au(111) the vast majority of graphene domains are locked into alignment with the substrate surface. The extraordinary extent of their orientational homogeneity is such that the resulting graphene film is a quasi-single crystal. The findings presented illustrate how metal species and crystal symmetry influence the structural properties of monolayer graphene. The selection of an optimal substrate for graphene growth can significantly reduce crystalline disorder in the resulting film.

Table of Contents

Chapter 6 Graphene Film Nanostructure

Chapter 7 Conclusion

References

Appendix A Graphene Growth on Alternative Substrates

Appendix B Numerical predictions of the C adatom gas concentration

List of Figures

Tables

List of Symbols and Abbreviations

ρ	Doping level
AFM	Atomic force microscopy
armchair	Edge-termination of graphene along <11>
ARPES	Angle-resolved photo-emission spectroscopy
CVD	Chemical vapor deposition
E_{gap}	Band gap size
fcc	Face-centered cubic
hcp	Hexagonal close packed
k_f	Fermi wave vector
LEED	Low-energy electron diffraction
LEEM	Low-energy electron microscopy
PMMA	Poly (methyl methacrylate)
PVD	Physical vapor deposition
R0	Orientation of graphene which is crystallographically aligned with the (111) substrate
R30	Orientation of graphene which is rotated 30º from alignment with the (111) substrate
SEM	Scanning electron microscopy
STM	Scanning tunneling microscopy
UHV	Ultra-high vacuum
XPS	X-ray photoelectron spectroscopy
zigzag	Edge-termination of graphene along <01>

Acknowledgements

I would like to extend my heartfelt appreciation to all the people who have helped to make my graduate career a success. First and foremost, I would like to thank Prof. Oscar Dubon, who has served as my research adviser. Prof. Dubon guided my career with patience, and encouraged me to grow as a person as a result. I would also like to acknowledge the contributions of Prof. Andrew Minor and Prof. Feng Wang for generously agreeing to serve on my dissertation committee. Another group of people who have been crucial to the progress of my research are my collaborators at the Sandia National Laboratories. Dr. Shu Nie, Dr. Elena Starodub, and Dr. Konrad Thürmer have all been integral to the graphene growth research presented here. I would like to specifically mention both Dr. Kevin McCarty and Dr. Norman Bartelt, also of the Sandia National Laboratories, for their mentorship as well as the vast amount of technical assistance they have generously provided. I thank my qualifying exam committee for their time and valuable input: Prof. Eugene Haller, Prof. Junqiao Wu, Prof. Andrew Minor, and Prof. Feng Wang. Of course, none of this would have been possible without David Hom. David has helped me with a multitude of administrative tasks with efficiency and remarkable good humor. And certainly no one has been more integral to my research than Jeff Beeman. I would also like to thank all the people I overlapped with in the Dubon and Haller research groups, and the EMAT program: Dr. Jeremy Robinson, Dr. Ian Sharp, Dr. Kirstin Alberi, Dr. Rouin Farshshi, Cesar Julaton III, Dr. Peter Stone, Dr. Nathan Miller, Dr. Robert Broesler, Marie Mayer, Holland Smith, Douglas Detert, Grant Buchowicz, Alejandro Levander, and Alex Luce. Most importantly, I would be remiss to not thank my friends and family for all their support. My relationships with Dr. Elizabeth Zimmermann, and Hal, Ben, Sue, Anne, and Cooper Wofford have been the bedrock supporting me throughout the last six years. Without your patience and understanding I would be nowhere. Thank you all.

Chapter 1 Introduction

The unique properties of graphene arising from its two-dimensional honeycomb structure make it a possibly transformative engineering material. The scientific novelty of these traits has long made graphene a focus of study for theoreticians [1, 2]. However, it was not until graphene was first isolated by Novoselov and Geim that the experimental validation of these theoretical predictions became possible [3-6]. Since that time a sustained research effort has been made to fully catalogue graphene's remarkable properties [7]. With many of its novel attributes now experimentally confirmed, it is imperative to identify improved graphene synthesis methods. It is this aspect of graphene research that this dissertation addresses.

Graphene consists of a monolayer of C atoms that are bonded into an sp^2-coordinated hexagonal crystal structure with *p6m* symmetry. The unit cell has a 2 atom basis and 2.46 Å lattice parameter, reflecting a C-C bond length of 1.42 Å (**Figure 1.1**). The remarkable strength of the in-plane C-C bonds makes graphene mechanically robust despite its single monolayer thickness. It may be manually handled without experiencing catastrophic damage although delicacy is required [8, 9]. Graphene is also largely chemically inert and can be stored in the ambient for extended periods without irreversible degradation [10].

Figure 1.1 Schematic diagram of the crystal structure of graphene. The hexagonal lattice of the monolayer thick, sp^2 bonded C crystal has a two atom basis. The unit cell is 2.46 Å on each side, with a 1.42 Å C-C bond length.

The significant properties of graphene are centered on its electronic dispersion. Ideal graphene is both a semimetal and a zero bandgap semiconductor because its valence and conduction bands are tangential at the charge neutrality point [3] (**Figure 1.2**). Near this point the bands are conical, resulting in a symmetric linear dependence between charge carrier energy and momentum. Electrons and holes occupying states where the conical bands meet – the Dirac point – have zero effective mass [4]. Thus charge carriers in graphene approximate a two-dimensional free-electron gas. In-plane mobilities up to 200,000 cm^2/V·s have been experimentally measured [11]. Most of the consequences of graphene's electronic structure, such as the room temperature manifestation of the quantum Hall effect [6], are outside the scope of this work.
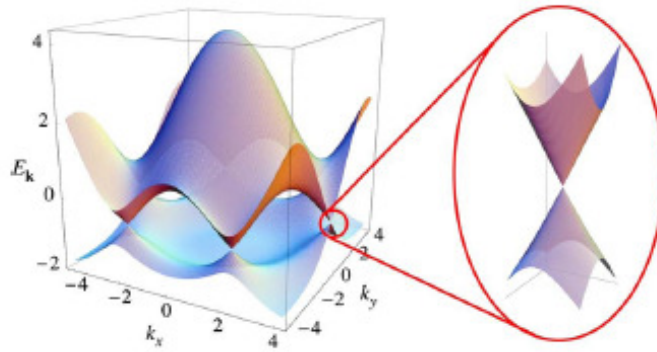
Figure 1.2 The calculated electronic dispersion of pristine graphene. The dispersion becomes linear near each of the six points of intersection between the conduction and valence bands (inset). Figure reproduced from [12].

A potentially useful consequence of the strict two-dimensional nature of graphene is its sensitivity to the local environment, specifically the ability to manipulate graphene's band structure by guiding its interactions with neighboring materials. These might be the substrate or additional over-layers added expressly for this purpose. An example of this phenomena is graphene grown on substrates, such as Ru or SiC, which interact strongly with the first graphitic layer [13, 14]. This bonding can be sufficient to eliminate graphene's linear dispersion and may even introduce sp^3 character into the C orbitals [15]. Of equal utility for future applications are the intrinsic thickness dependent properties of graphene itself. It has been shown that bilayer graphene may be manipulated to open a small bandgap [14, 16, 17]. More nuanced bandgap engineering may be accomplished by controlling the relative orientation of layers in a graphene stack [18, 19]. The properties of graphitic films continue to evolve until they approach those of bulk graphite at approximately 10 layers [20]. The sensitivity of graphene to its local environment gives it further versatility as an engineering material.

Manipulating graphene into device architectures requires the development of a comprehensive set of processing techniques. For some applications this process has already started. The ability to induce both *n*- and *p*-type doping is a requirement in microelectronics. Graphene has been doped with both electrons and holes using surface absorbates [21, 22]. A more attractive approach is the integration of dopant atoms into the C lattice [23], although further development is required. Lithographic patterning of graphene has allowed for the geometrically complex structures required for microelectronics. The consequences of laterally constricting graphene have been studied this way [24], as well as a variety of device arrangements [25, 26]. A further processing procedure proven to be compatible with graphene is surface functionalization. The adhesion of reactive functional groups to the surface of graphene has been used to create chemical and biological sensors [27, 28]. As these and other processing methods mature they will allow graphene to be integrated into increasingly complex devices.

Despite the processing and fabrication challenges, a number of graphene based demonstration devices have been manufactured. These generally exclude logic and digital based functionalities due to the low on-off ratios of graphene based transistors. However, the low power consumption and fast response time of graphene transistors

makes them ideal for analogue applications, such as high frequency signal processing and amplification [25]. Graphene's device potential is not limited to microelectronics. The aforementioned chemical and biological sensors are one example of this [29]. Another is the extremely high Q-factor drum resonators facilitated by the exceptional mechanical properties of graphene and graphene derived materials [26]. More ambitious proposals include all C integrated circuits exploiting the thickness dependence of graphene's properties. Bi-layer graphene might serve for transistor channels, with monolayer material used for device interconnects. While such schemes remain impractical, they do serve to illustrate the surge in technological interest that has accompanied the physical isolation of graphene.

The progress achieved in graphene research attests to the ability of experimentalists to adapt to materials constraints. Current limitations in graphene synthesis force choices between film size, crystalline quality, uniformity, and processability. Selection of the most appropriate synthesis method for a particular application may mitigate the detrimental impact of these shortcomings. For instance, most ultra-high charge-carrier mobility devices are fabricated from exfoliated graphene flakes which are only ~100 μm across [11]. Those requiring larger films are limited to the lower quality polycrystalline graphene grown on Cu foil substrates [30]. A synthesis routine which combines the crystalline quality yielded by mechanical exfoliation with the film size facilitated by CVD would alleviate the need for compromise. This is the objective of graphene synthesis research.

Graphene synthesis takes place in a different regime than traditional thin-film growth (mechanical exfoliation is a different scenario all together). Standard thin films are of finite thickness and are separated from their environment by two material interfaces. Graphene is itself effectively an interface. Indeed, the surfaces of graphene are integral parts of the material and endow it with valuable properties. π states, which protrude in the out-of-plane directions, are responsible for its linear dispersion and other pertinent electronic behaviors. The applicability of the framework of traditional thin-film growth is reduced by graphene's two-dimensional nature. The fact that graphene growth propagates within the plane of the film, as opposed to perpendicular to it, demonstrates this fundamental difference.

Meaningful improvements in graphene synthesis require understanding not only its specific peculiarities but also the fundamental processes that underpin two-dimensional epitaxy. This dissertation examines these essentials by studying the nucleation and growth of graphene on Cu(100), Cu(111), and Au(111). Cu and Au are optimal substrate materials to inspect because their low C solubility allows them to support monolayer graphene growth. By using LEEM to examine the substrate surface during growth we are able to observe the sub-monolayer evolution of the films. These experiments allowed us to investigate the influence of substrate symmetry and composition on the properties of the resulting graphene films. Understanding these parameters will help the growth community meet the increasing demand for high quality graphene films.

Chapter 2 Graphene Growth on Metal Substrates

2.1 Chronological evolution of methods for graphene growth on metals

An ideal graphene synthesis method remains elusive, but the past few years have seen significant progress towards that objective. This research has progressed along multiple parallel paths. The thermal decomposition of SiC [31], and the solution processing of partially oxidized graphene flakes are two of these directions [32]. A third, graphene growth on metal surfaces, shows perhaps the most promise of all. This synthesis technique has progressed to the point that it now produces arbitrarily large graphene films which are almost uniformly a single monolayer thick [30]. Advances in graphene growth on metal surfaces have been achieved primarily through empirical optimization. While successful, this has left many fundamental questions uninvestigated.

Graphene has long been studied as a contaminant in catalysis. However, it was not until the work of Sutter *et al.* regarding graphene grown on Ru that the significance of these observations became apparent [13]. The efforts of McCarty *et al.* with graphene growth on Ir and Ru closely followed [33-37]. These studies were fundamental in nature, and did not focus on generating graphene films for device applications. Two facts changed to increase the potential of graphene grown on metals for use in devices. First, Ni was adopted as an alternative substrate [8]. This substantially reduced both the cost and practical difficulty of growing graphene on metals. Secondly, and perhaps more importantly, a suitable process for transferring graphene films from their metal substrate to a dielectric support was developed [8, 38]. The general procedure is to dissolve the metal using an appropriate etchant after supporting the graphene film with a polymer layer, usually PMMA. The graphene film-polymer support can then be placed on the desired final surface and the polymer subsequently removed. Unfortunately, graphene grown on Ni is not homogeneously thick [8]. The metal also forms an intermediate surface compound with C. These factors ultimately make Ni a less than ideal substrate for graphene growth.

2.2 Monolayer graphene growth on Cu

In 2009 Li *et al.* addressed many of the shortcomings manifested by graphene growth on Ni by switching to Cu substrates [39]. The method developed by Prof. Ruoff's team is still commonly followed with only minor revisions. It uses polycrystalline Cu foils of relatively low purity as the substrate. Carbon is introduced to the Cu surface by flowing methane across it at elevated temperatures (ethylene is now more commonly used as the C precursor). This process yields films which are almost exclusively a monolayer thick. Furthermore, the insensitivity of the film thickness to methane exposure time reflects a self-limiting growth process. With only limited optimization this procedure resulted in films with measured mobilities of 4050 cm^2/V·s [39]. A sub-monolayer graphene film grown using this method is shown in **Figure 2.1**.
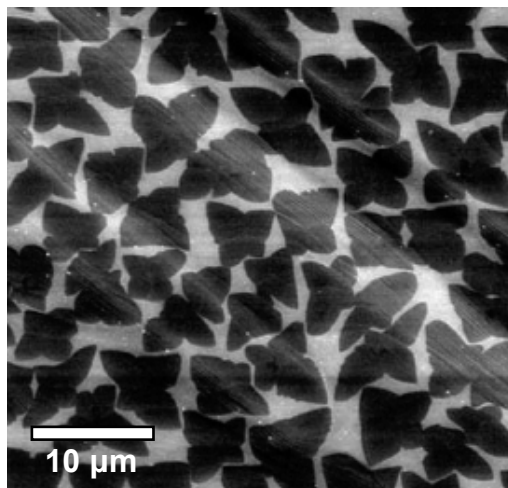
Figure 2.1 Scanning electron microscope image of graphene islands (darker regions) grown on a Cu foil by CVD. Notice the pronounced four-lobed shape of the islands, and the alignment of the lobe axes from island to island. Image reproduced from [40].

The ability of Cu to support monolayer graphene growth points to a fundamental difference between it and Ni. Prof. Ruoff and his group identified the origin of this behavior through selective isotope labeling [41]. The quantity of C that dissolves into the bulk of Cu during growth is limited by its negligible solubility. In contrast, Ni has a finite C solubility of a few percent at the temperatures of interest. Ni thus develops a C reservoir within its bulk as C is deposited. The precipitation of this reservoir during sample cooling severely degrades the control which may be exerted over the C film thickness [8]. The absence of a C reservoir in Cu substrates was confirmed in the work presented here. Graphene chemically passivates the Cu surface once it is covered, preventing further hydrocarbon decomposition [41]. Because hydrocarbon decomposition is halted and no C reservoir forms, controllable monolayer growth is possible.

Although the chemical vapor deposition of C through hydrocarbon decomposition has come to dominate, it is not the only suitable method to dose metallic substrates with C. Physical vapor deposition of elemental C is also an effective way to synthesize graphene on metals. Evidence shows that, at least in some circumstances, the origin of C does not influence graphene growth behavior. Graphene grown under the same conditions on the same Ir crystal showed no discernable variation depending on the source of C, be it chemical or graphite [34]. Additionally, the results presented here for graphene grown on Cu by PVD are consistent with reports for CVD growth [42]. The decoupling of graphene growth behavior from the origin of C suggests that growth processes are not controlled by precursor chemistry. The findings presented here reinforce this statement.

2.3 Metal substrates

Interactions between surface atoms of metal substrates and C can profoundly influence both the growth kinetics and final structure of graphene films. This is tangibly

illustrated by comparing graphene growth on Ru and Pt. Ru exerts significant influence on the C film [13] while the impact of Pt is relatively muted [43]. Preobrajenski *et al.* have shown that there is a higher degree of orbital hybridization between graphene states and the 4d states of the Ru(0001) surface than there is with the 5d states of Pt(111). As mentioned previously, the graphene-Ru(0001) bond approaches a covalent one [15]. The variation in bond strength between graphene and the Ru and Pt manifests itself in a number of different ways. Graphene grown on Ru(0001) is strictly limited to a single rotational orientation on the surface while on Pt(111) it may adopt a range of relative orientations. Perturbations in the electronic structure of graphene can also result from its interactions with metallic substrates. Pt substrates largely preserve the characteristic linear dispersion of free standing graphene [43]. The coupling between monolayer graphene and Ru is sufficient to completely eliminate it [15]. Metal substrates may also influence graphene in more subtle ways, such as altering the free energy associated with different graphene edge terminations. Sub-monolayer graphene islands on Ru(0001) have smooth edges [13] whereas they form strongly faceted shapes on Pt(111) [43]. Because the edges of graphene sheets bind with the substrate, their energetic anisotropy is very much influenced by the metal. In addition to governing the bonding between graphene and metal, the substrate surface chemistry may influence graphene growth in other ways.

Graphene is not the only C species with which the metal substrate interacts. There are also C adatoms and a variety of different adatom clusters on the surface. The time C adatoms spend on the substrate prior to incorporation into a graphene crystal introduces an entire additional set of C-metal interactions which are inherent to graphene growth. The diffusion behavior of this mixture of C species on a particular metal substrate is intimately tied with graphene growth as will be discussed in Chapter 4. The choice of metal substrate also plays a role in determining the growth mode of graphene. Graphene growing on Ru again provides an illustrative example. Rather than by the attachment of individual C monomers, graphene growing on Ru(0001) extends by joining ~5 C atom clusters [33]. The concentration and lifetime of these larger C clusters is determined by their stability on the Ru(0001) surface. Finally, the characteristics of a particular metal substrate establish how multilayer graphene may form. If the solubility of C in the bulk of the metal is sufficiently low, monolayer growth may be stable. There is also variability between higher C solubility metals in this regard. Additional layers of graphene on Ru only begin to form as the first layer nears completion [13]. They may also grow congruently with the initial layer as occurs on Pt [43]. These factors show the dependence of graphene's growth behavior on the chemistry of the metallic substrate.

2.4 Metal substrates: Symmetry

The symmetry of metal substrates used for graphene growth is another influence on both the evolution and final structure of the C film. The impact of substrate symmetry has not been explored to the same degree as the chemical interaction between the graphene and metals. This is perhaps unsurprising. Traditional thin-film growth generally uses substrates that match the symmetry of the desired film. As a result the

majority of in-depth growth studies have used close packed substrates which most closely mirror the symmetry of graphene [12, 32-35][44]. Ubiquitous to graphene grown on close-packed substrates are moiré patterns in the film. The periodicity of the moiré supercell is determined by the lattice mismatch between the graphene and metal, their relative orientation, and the degree of geometric distortion imposed on the two materials. The most exhaustively studied example is the moiré formed by graphene on the symmetry matched (0001) surface of Ru. Each moiré supercell contains 25 x 25 graphene unit cells and is composed of 2 x 2 crystallographically inequivalent subcells [45]. The restriction of graphene to a single orientation relative to the Ru surface facilitates such a complex superstructure. Although there are many more studies of graphene growth on symmetry matched surfaces, there are a few reports regarding non-close packed crystal facet substrates. Such studies hint at a broad range of previously unreported behaviors.

Graphene develops an assortment of different morphologies on non-(111) or (0001) metal substrates. Disordered polycrystalline Ni films provide an interesting opportunity to observe the structure developed by graphene on multiple crystal facets. On the (111) surface the C film forms the familiar moiré pattern with a 22 Å periodicity. However the (110) facet alters the superstructure into a striped configuration [46]. Interestingly, graphene domains were observed to extend from one Ni facet to another. In these instances a single graphene crystal displays multiple moiré patterns depending on the facet on which it rests. Another example of substrate symmetry impacting graphene is during its growth on Cu(100). Graphene islands develop a peculiar four-lobed shape, the long axes of which align from island to island, as is shown in **Figure 2.1** [40, 42]. This example illustrates how substrate symmetry influences the sub-monolayer evolution in addition to the final structure of the film. The specific scenario of graphene growth on Cu(100) will be explored in detail in Chapter 4. Although there is not yet a systematic understanding of the role that substrate symmetry plays in growth, the reports which do exist establish this as an important consideration in the continued development of graphene synthesis. By selecting low C solubility substrates with different surface chemistries and symmetries this dissertation methodically explores the influence these properties have on graphene growth.

Chapter 3 Details of Graphene Growth on Cu(100), Cu(111), and Au(111)

3.1 Substrate selection and preparation

This dissertation comprises experiments designed to systematically explore the influence of substrate material and symmetry on graphene growth. Substrates composed of two different materials and symmetries were selected: Cu(100), Cu(111), and Au(111). Au also supports monolayer graphene growth because it has a similarly low bulk C solubility to that of Cu. The stipulation that the substrate materials selected must allow monolayer graphene growth was enforced for multiple reasons. It is the interplay between the initial monolayer of graphene and the metal substrate that is the objective of this study. Additional C beyond the first monolayer of graphene introduces additional complexity during characterization. The interactions between a metal substrate and the second and third layers of graphene are significantly different than those with the first [47]. Finally, precise thickness control of graphene films is a prerequisite for applications, be they one or two monolayers thick. This makes low C solubility substrates much more likely to be of technological value. The Cu and Au substrates selected allow us to isolate the influence their different elemental makeup and surface symmetries have on graphene growth.

By growing graphene on both the (100) and (111) facets of Cu we are able to observe directly the influence of surface symmetry. The (100) surface of Cu has four-fold symmetry with a square surface unit cell 2.56 Å on a side (symmetry group *p4m*) [48]. Cu(111) is six-fold symmetric with the same 2.56 Å lattice parameter (symmetry group *p6m*, although this is reduced to *p3m* if sub-surface atomic layers are significant). Comparing the growth behavior and resulting film structure of graphene on Cu(111) and Au(111) removes surface symmetry as a variable. This will instead expose the consequences of changes in substrate composition. While it has the same symmetry as Cu(111), Au(111) has a larger surface unit cell with a 2.88 Å lattice parameter [49]. The possible consequences of the larger substrate unit cell are also of interest. The combination of Cu(100), Cu(111), and Au(111) substrates provides complementary comparative studies.

The Au(111) and Cu(111) substrates used were commercially purchased single crystals. Prior to growth experiments, both crystals were extensively outgassed in UHV. In order to further improve the surface quality, the crystals were cleaned and smoothed using O and Ar sputtering in conjunction with high temperature annealing in UHV (up to approximately 1000 ºC). The crystals were recycled for use in multiple growth experiments by burning the graphene films off with O_2 at high temperature. Further sputtering with both O and Ar and ~1000 ºC annealing was also used. This cleaning cycle fully restored the crystal surfaces to their condition prior to the initial deposition of C, an example of which is shown in **Figure 3.1**.

Unlike the (111) oriented Cu and Au, the Cu(100) substrates examined were constituent grains of polycrystalline Cu foils. The commercially purchased Cu foils were 25 μm thick, 99.999% pure Cu (Johnson Matthey, catalogue #10950). Prior to C
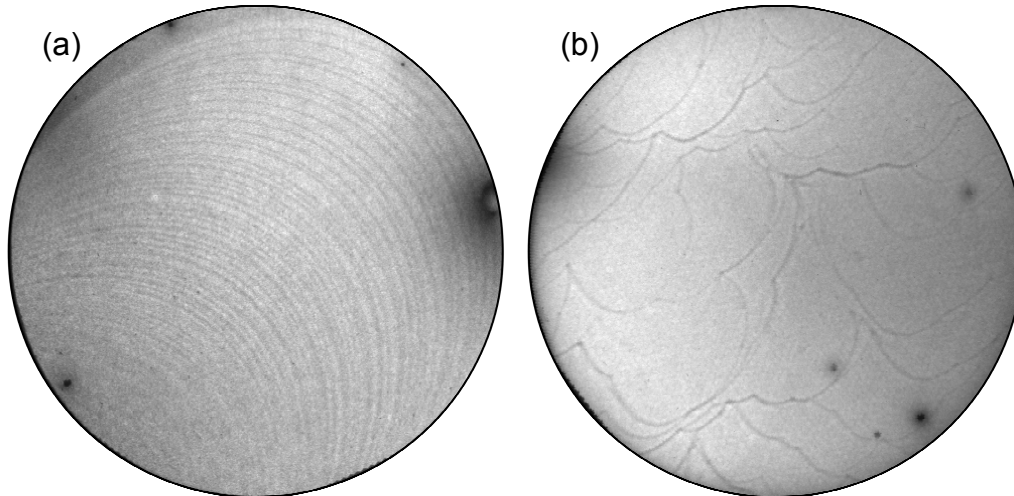
Figure 3.1 Low-energy electron microscope micrographs of bare Cu(100) (**a**) and Au(111) (**b**) substrates prior to the growth of graphene. Substrate steps, which are the faint lines in both images, are highly mobile at the temperatures necessary for growth due to the evaporation of the metal. The mobile steps may become pinned at surface features, which can be seen on Au in **b**. (FOV is 14.5 μm in **a**, and 9 μm in **b**).

deposition, the Cu foil was annealed in a tube furnace at 1000 ˚C for 45 minutes in an Ar-H_2 mixture at atmospheric pressure, which served to reduce the surface oxide. Samples were then transferred in air to a UHV chamber having a base pressure of ~1×10^{-10} torr, where they were annealed again at ~960˚C for 10 minutes and subsequently cooled to the growth temperature. Pre-growth low-energy electron diffraction (LEED) analysis of the Cu surface which results from this annealing treatment shows a strong (100) in-plane texture. The (100) texture is characteristic of Cu foils manufactured by a cold-rolling process, and recrystallized by subsequent annealing [50]. Indeed the surfaces of many Cu grains showed remarkably precise alignment with the (100) plane. The spacings between single Cu atomic steps was often greater than 100 nm, indicating surface normals less than 0.1º from the [100] azimuth (**Figure 3.1.a**). This degree of alignment rivals or exceeds the surfaces typically obtained by cutting and polishing single crystals. Individual Cu grains within the foils reached sizes as large as ~1 mm. Unlike with the single-crystal, (111) substrates, the Cu foils were not cleaned and reused for multiple growths; a new sample was introduced to the growth chamber for each experiment.
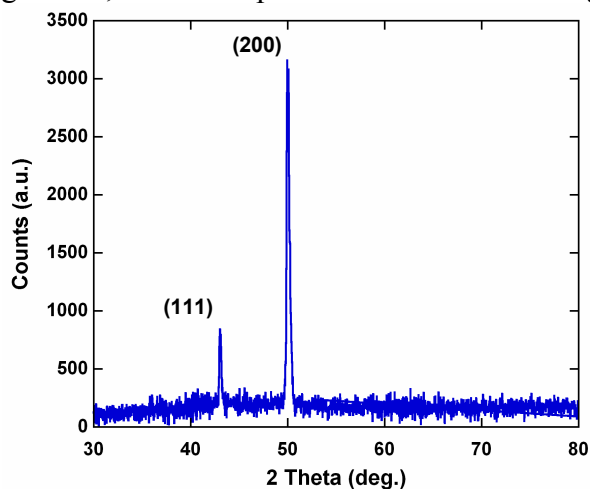
Figure 3.2 X-ray diffraction from the Cu foil commonly used as the substrate in the graphene growth process developed by the research group of Prof. Ruoff. The prominent (200) peak shows the highly-ordered, (100) texture of the polycrystalline foil. This type of texturing is typical for foils formed by cold-rolling.

A further intention of using a Cu foil substrate was to approximate the commonly used CVD growth procedure developed by the Ruoff research group at the University of Texas, Austin [34]. The Cu foil used here had higher purity than the Alfa Aesar foil used by Ruoff (item #13382): 99.999% as opposed to 99.8%. Growths were also performed on the Alfa Aesar foils, but the higher levels of surface impurities and smaller Cu grains prevented useful imaging of the surface (see Chapter 2.3). Despite the differing surface quality, the two types of foils have important similarities. First, x-ray diffraction shows that annealed Alfa Aesar foils have the same (100) in-plane texture as the foils studied here (**Figure 3.2**). Thus, graphene is growing on Cu(100) crystallographic facets for both types of foil. Secondly, similar graphene island morphologies can be seen in sub-monolayer films on both types of foils, suggesting that the growth mode is not altered by foil purity (see Chapter 4). These mutual properties imply that the growth behavior of graphene on Cu(100) observed here is common to the Ruoff process.

3.2 Growth details

All growths were performed in UHV at a base pressure of $\sim 1 \times 10^{-10}$ torr. C was evaporated from an electron-beam heated graphite rod mounted in the UHV chamber. It was necessary to use physical vapor deposition in these studies. Exposure of both Cu and Au substrates to ethylene at pressures below 10^{-7} torr did not result in appreciable C adsorption. As was discussed previously, similar growth behavior in graphene has been observed regardless of the C source, be it CVD from a hydrocarbon precursor or PVD of elemental C [42]. The elemental PVD process used here afforded excellent control over the C flux and graphene growth rate. Complete graphene monolayers were grown over the course of 10 to 30 minutes. These relatively slow growth rates were important as the sub-monolayer evolution of the film was of particular interest. Graphene was grown by this process over a range of different substrate temperatures from 690 ºC to 975 ºC, which were measured by a thermocouple on the substrate mount. Samples were cooled to room temperature at ~50 ºC per minute immediately following the completion of growth.

3.3 Primary characterization – Low-energy electron microscopy

Graphene films were synthesized in the chamber of a low-energy electron microscope. This served as the primary characterization tool for these studies as it allowed for the real-time monitoring of the sample surface. A LEEM can maintain imaging from UHV up to pressures in the $\sim 10^{-7}$ torr range. The physical structure of the microscope, as shown in the schematic in **Figure 3.3**, comprises two electromagnetic lens stacks to either side of an electron beam separator. The beam separator bends the current and guides it to and away from the sample surface. Low-energy electron microscopy (LEEM) is a "cathode lens" technique, meaning the electron gun and sample are held at approximately the same potential [51]. This causes the electrons to decelerate from 15-20 keV between the separator and the sample surface. The final energy with which the electrons interact with the sample surface is generally tunable between 1 and 100 eV.

electron gun

illumination optics

objective lens

sample

beam splitter

condenser optics

detector
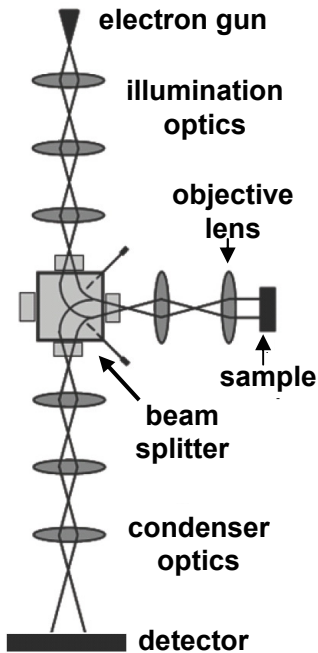
Figure 3.3 A schematic lens diagram of a low-energy electron microscope. In cathode lens electron microscopes such as these, the imaging electrons decelerate between the objective lens and sample surface, where they interact at 1-100 eV.

LEEM is an extremely surface sensitive form of microscopy. Interactions between the 1-100 eV electrons and sample surface are limited to the first few layers of atoms. The primary source of contrast from these interactions is diffraction [51]. Despite its surface sensitivity LEEM does allow for the extraction of some depth related information. These "intensity-voltage" measurements are taken by varying the energy of the imaging electrons while monitoring the image intensity. This essentially measures the electron reflectivity of the surface as a function of energy. Intensity-voltage measurements, or "I-V" measurements, are one way to confirm the number of graphene layers which have formed on a surface. LEEM resolution is usually limited by the homogeneity of the electric field between the cathodic lens beam splitter and the sample surface [51]. This is particularly true when the sample surface is not absolutely flat. Surface protrusions and roughness distort the decelerating field and reduce image resolution. Problems may also develop when imaging at the exact interface between two materials because a difference in work function causes a similar disruption.

Despite these limitations LEEM is a powerful characterization tool. The ability to monitor the graphene as it propagates across the Cu and Au substrates in real-time is particularly valuable. LEEM reveals a number of important aspects of graphene growth in addition to the morphological evolution of the C film itself. It allows the surface quality of the substrate to be evaluated prior to growth. The location and type of graphene nucleation event can also be observed. Propagating graphene growth fronts have potentially significant interactions with mobile substrate step edges, dynamic behavior well documented by LEEM. Finally, LEEM gives instantaneous feedback as to the degree of coverage graphene has achieved and shows precisely when a complete monolayer has formed.

The LEEM used in these experiments enables analysis by low-energy electron diffraction (LEED). LEED yields information about the crystalline structure of both the graphene and metal substrate. This allowed the determination of whether a C film was indeed crystalline graphene. LEED was also useful in monitoring the Au(111) herringbone surface reconstruction (see Section 6.3). Perhaps most importantly, the important factor of the relative orientation between the two materials is also revealed by LEED. The combination of LEEM and LEED allows the correlation of growth kinetics and substrate interaction with the crystallography of the system.

3.4 Supplementary characterization techniques

In addition to *in-situ* LEEM and LEED, a number of other *ex-situ* methods were used to characterize graphene growth on Cu(100), Cu(111), and Au(111). Scanning tunneling microscopy (STM) was used to observe directly the atomic-scale structure of the graphene and metal surfaces. This was particularly useful in identifying superstructures such as moirés. Graphene generates a strong Raman signature, which was used to confirm the presence of graphene and to estimate its crystalline quality [52]. Some of the results of graphene growth on these metals were observable by optical microscopy, which gave quick and convenient insight into the state of the graphene film and underlying metal surface. X-ray photoelectron spectroscopy usefully eliminated the possibility of any contaminants being present, and gave information on the C bonding. Finally, angle-resolved photoemission spectroscopy (ARPES) was used to evaluate the electronic structure of the graphene-metal heterostructure. When combined with LEEM, these methods allowed the systematic evaluation of graphene growth on Cu(100), Cu(111), and Au(111).

Chapter 4 Graphene growth

4.1 Nucleation behavior

Graphene islands display a range of different nucleation behaviors depending on the substrate surface. These included both homogeneous and heterogeneous nucleation. In this study homogeneous nucleation refers to the formation of graphene from carbon vapor on a pristine substrate terrace, while heterogeneous nucleation involves a distinct feature on the substrate, such as a foreign particulate or substrate step edge. Graphene nucleated immediately upon the start of C deposition on all three surfaces, Cu(100), Cu(111), and Au(111). Efforts were made to directly measure the concentration of the adatom gas on the substrate by monitoring the electron reflectivity of the non-graphene covered portions as a function of time. This procedure has previously been used to determine the surface concentration of the C adatom gas during graphene growth on both Ru and Ir [33]. No variation in reflectivity could be detected during C deposition on Cu(100), Cu(111), or Au(111), indicating the C adatom gas concentration never reaches the detection threshold for this technique. Together these facts suggest the steady-state concentration of the C adatom gas is extremely low during graphene growth. Likewise, graphene nucleates on Cu(100), Cu(111), and Au(111) at a sufficiently low C surface concentration to not detectably alter the electron reflectivity.

In the case of graphene growing on Au(111), islands were observed to nucleate both homogeneously and heterogeneously. The primary heterogeneous sites were Au step edges. An average overall nucleation density of 7.5×10^{8} nuclei per cm^{2} was observed. This high nucleation density could be a result of a small stable graphene nucleus size, or of a large energetic benefit for a C atom to move from the adatom gas into a graphene crystal. In comparison, graphene nucleation on Cu(100) was dominated by heterogeneous nucleation. However, it took place at a much lower density of $\sim 1.3 \times 10^{6}$ nuclei per cm^{2}. It is difficult to extract details regarding the types of surface features which stimulate heterogeneous graphene nucleation on Cu(100) because of their small size. These sites remained easily visible despite their size due to their tendency to act as strong pinning sites for mobile Cu step edges. Because of this step pinning, graphene islands nucleating on Cu(100) often do so on a significant step bunch.

Both heterogeneous and homogeneous graphene nucleation was observed on Cu(111). Similar to Cu(100), primary graphene island nucleation on Cu(111) is almost exclusively heterogeneous. Additional nucleation could be induced at a later time via a rapid increase in the C flux. Interestingly, this secondary nucleation tends to occur homogeneously, and at locations roughly equidistant from existing islands. These two facts strongly suggest adatom surface concentration is significant in secondary nucleation. This was confirmed by comparing the locations of secondary nucleation with an approximate map of the adatom surface concentration. The adatom surface concentration was estimated using the geometric distribution of existing islands immediately prior to secondary nucleation to set boundary conditions for the diffusion equation. Existing islands were modeled as perfect C sinks, while the edge of the field of view was treated
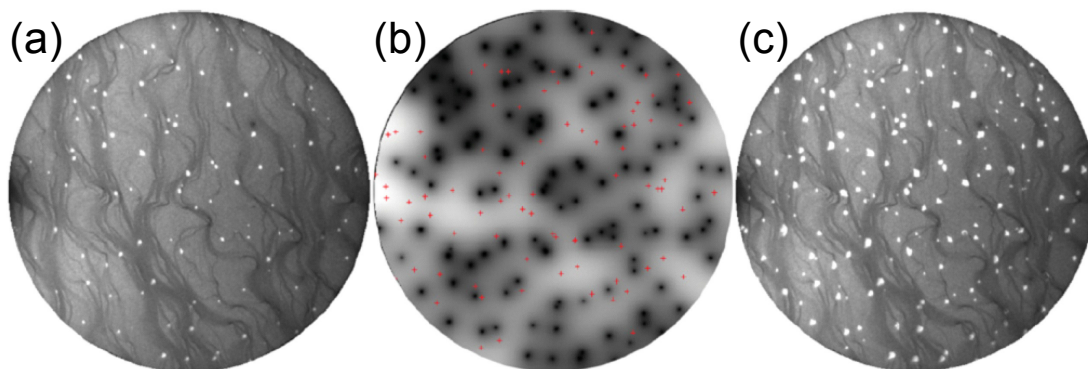
Figure 4.1 (a) LEEM image showing an array of graphene islands during growth at 894 ºC (46 μm field of view). **(b)** Carbon adatom and ad-species concentration calculated from the diffusion equation for the given surface geometry, where bright regions have a high concentration, and darker regions have a lower concentration. A constant incident flux was assumed, each island boundary was treated as a perfect sink, and the edge of the field-of-view was considered a perfect mirror. **(c)** Experimental configuration after secondary islands nucleated following a sharp increase in the C flux. The location of secondary nucleation events (red crosses in **b**) show reasonable correlation with the regions of predicted high C surface concentration. The author would like to acknowledge Dr. Norm Bartelt of Sandia National Laboratories.

as a mirror. The results of this simulation can be compared with experiment in **Figure 4.1**. The two show a high degree of correlation. Thus while primary graphene nucleation on Cu(111) is determined by the distribution of surface defects, any subsequent nucleation is the result of a local maximum in the C adatom surface concentration. Graphene nucleation may be stimulated by both surface imperfections and local regions of high C adatom concentration.

4.2 Growth Mode

By observing the morphological evolution of graphene films on Cu(100), Cu(111), and Au(111) by LEEM we are able to determine their growth mode. Furthermore, we may establish those factors which govern the growth mode. In each of these cases it is the kinetics of the growth reaction which dominate. On Cu(100) the attachment kinetics of C atoms, or atom clusters, at the edge of the graphene crystal determine the growth behavior. This is in contrast to graphene growth on both Cu(111) and Au(111) where diffusion of C upon the substrate surface dictates the particulars of growth. Which growth mode graphene undergoes determines not only the shape of individual islands, but also has important consequences for the properties of the resulting continuous film.

4.2.1 Attachment limited growth – Cu(100)

Graphene islands growing on Cu(100) are initially compact in shape. Over time each becomes increasingly ramified until it develops the distinct lobed structure shown in **Figure 4.2.a-d**. Islands reach a steady-state shape with four branches and, allowing for irregularities, this shape is eventually obtained by every graphene island. Interestingly, the long axes of the graphene lobes tend to align from island to island, as is shown in
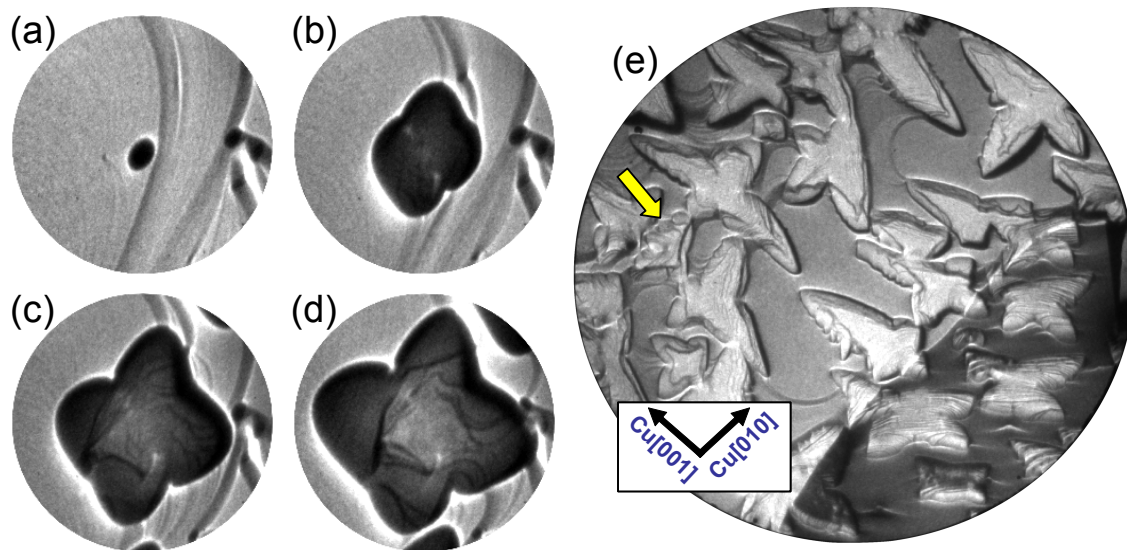
Figure 4.2 LEEM micrographs recorded 15 (**a**), 90 (**b**), 240 (**c**), and 390 seconds (**d**) after the start of deposition of C onto a (100) oriented grain of a polycrystalline Cu foil (FOV = 10 μm, grown at 842 ºC). The shape evolution of graphene islands on this surface results in the development of a characteristic four-lobed island morphology. Allowing for slight variations, this shape is seen in all graphene islands on this surface, as can be seen in **e** (grown at 790 ºC, FOV = 46 μm). Notice the directions of lobe axis alignment correspond with Cu<001> in-plane directions, although there is some variability due to growth interruptions, such as large Cu step bunches or inter-island impingement (yellow arrow).

Figure 4.2.e. Each axis is close to a Cu<001> in-plane direction although there is sometimes substantial deviation. Graphene islands were observed to grow across grain boundaries within the Cu foil. Islands that continued growing after crossing a Cu boundary did so at a slower rate. Despite their irregular shapes the graphene islands eventually combine to form a complete polycrystalline film. The spaces between islands fill progressively more slowly after initial inter-island impingement occurs.

Why the graphene islands should form with four lobes is puzzling. Island shapes which are governed by the minimization of the free energy associated with their termination must have a concave shape according to the Wulff construction [53]. This is not the case for graphene islands on Cu(100). A clue to this dilemma is provided by a careful diffraction analysis of individual graphene islands, as is shown in **Figure 4.3**. Selected-area diffraction from each lobe of individual islands show that they are not composed of a single orientation of graphene. Instead each lobe is composed of graphene whose lattice is rotated differently about the surface normal. We are able to ascertain the spatial distribution of these rotational variants using dark-field LEEM in the first-order diffraction condition of the graphene. Each constituent crystal meets at the approximate geometric center of the island. This would suggest they share a common nucleation event, which is consistent with observations made during growth. Some islands have a more convoluted distribution of rotational variants, perhaps as the result of multiple spatially close nucleation events. The distribution of crystalline domains within each graphene island explains how it is possible for them to adopt a four-lobed shape.

15
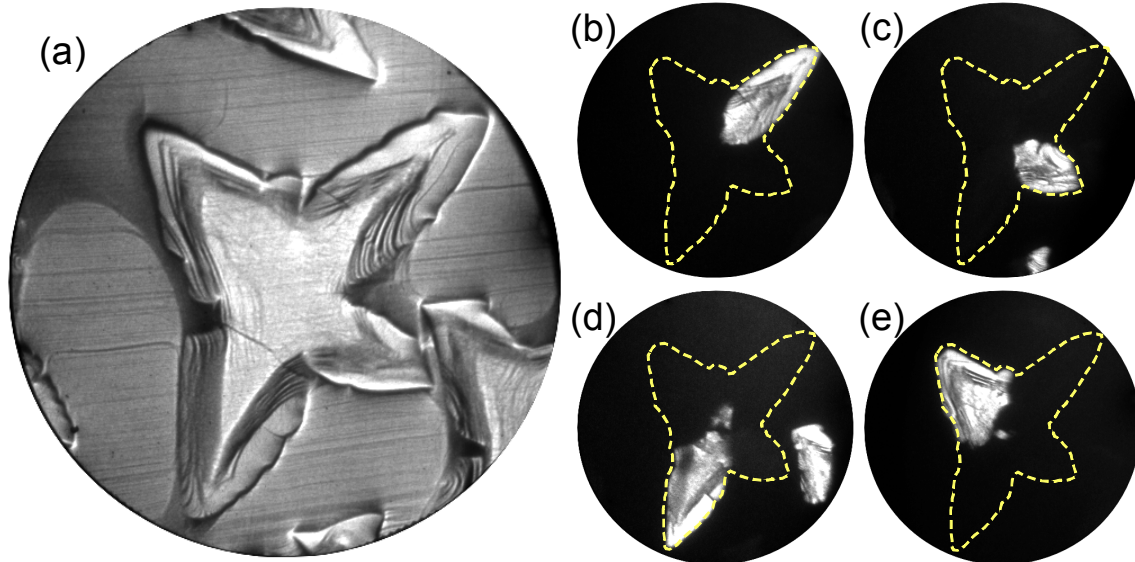
Figure 4.3 Bright (**a**) and dark-field (**b-e**) LEEM micrographs of a large graphene island grown on a (100) oriented grain of a polycrystalline Cu foil. Each graphene island is composed of multiple constituent crystals, the spatial distribution of which can be seen in (**b-e**). The graphene (01) direction is rotated by 28º (**b**), 2º (**c**), 8º (**d**), and 42º (**e**), relative to Cu<001> (FOV = 20 μm, grown at 790 ºC, yellow dashes are the approximate island boundary).

The highly anisotropic elliptical shape of each individual lobe, as shown in **Figure 4.3.a**, is remarkable. It is possible to determine whether this lobe shape is the result of edge energy minimization or whether it is a consequence of growth kinetics by monitoring the profile of a lobe as a function of time. In the simplest kinetically controlled growth model, the growth rate is a function of orientation solely. As shown by Frank [54], systems with an angularly dependent growth velocity exhibit a characteristic behavior. Consider a given point on the crystal edge, as defined by its particular edge normal. As the crystal edge advances, the succession of points with the same edge
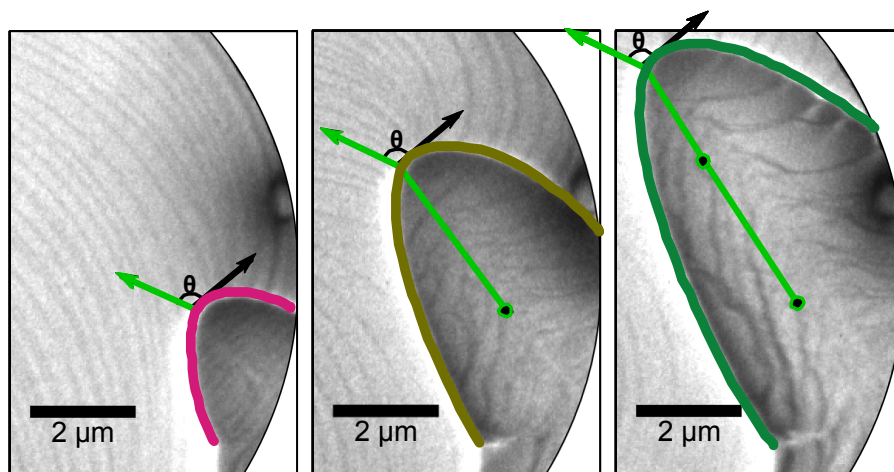
Figure 4.4 LEEM micrographs/schematic displaying a technique for extracting the growth trajectory of a point on the perimeter of a crystal. A point is defined by the angle of its edge normal. After marking its location, the movie is advanced, and the point on the perimeter with the same edge normal is marked. Iterating this procedure – with a smaller time step that shown here – yields the growth trajectory of that particular point on the crystal perimeter (images separated by 360 seconds of growth).

16
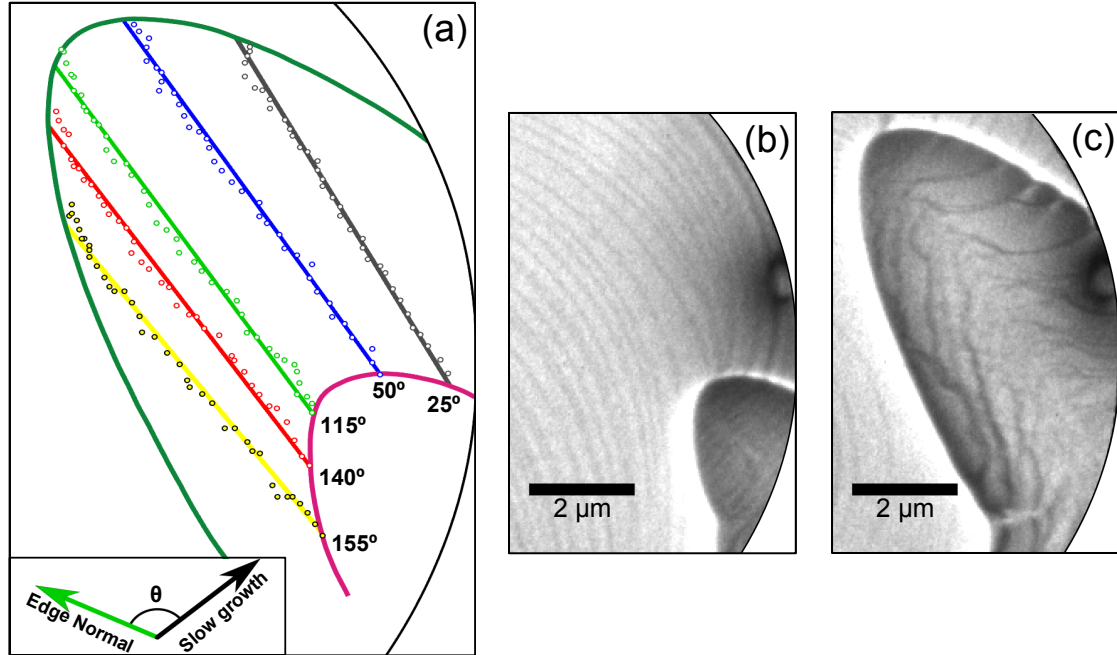
Figure 4.5 Growth trajectories (**a**), for a range of different edge orientations, extracted from LEEM micrographs (**b,c**) of graphene growing on Cu(100). The lobe at time **b** is outlined in purple in **a**, while time **c** is outline in dark green. A growth rate that is solely a function of orientation will result in a linear growth trajectory for a point on the crystal edge with a given normal, as shown in **a** for five points defined by normals of 25º (gray), 50º (blue) 115º (green), 140º (red) and 155º (yellow) relative to the slow-growth direction. The colored dots are extracted locations, while the solid lines are fits. The excellent agreement between the data and fits demonstrates the linearity of the growth trajectories for given graphene edge orientations.

normal will follow a linear trajectory (**Figure 4.4**). **Figure 4.5** shows and example of the results of this type of analysis for a lobe that grew unperturbed by neighboring islands or surface imperfections. Each orientation of this lobe's growth front moves along a line as the lobe tip propagates over a distance of 8.5 μm. This behavior was found for all twelve of the other freely growing lobes analyzed from growths conducted at 790˚C. The linearity of the growth trajectory over a substantial range of island sizes demonstrates that a well-defined angularly dependent growth velocity exists for each lobe.

As the growth progresses these kinetics will eventually yield a steady-state shape for each lobe. The shape can be determined from a variation of the Wulff construction by substituting the angularly dependent growth velocity for the surface-energy anisotropy [54](**Figure 4.6**). To see what sort of anisotropy is required to generate the shapes we observe, we examined a simple model of the growth velocity. For a six-fold symmetric crystal growing on a four-fold symmetric substrate, in general, the growth velocity will have two-fold symmetry. A simple two-fold symmetric model is:

$$v(\theta) = (1+r) + (r-1)\cos(2\theta)$$ **Equation 1**

where v is the growth velocity, θ is the angle of the edge normal relative to the slow-growth direction, and r is the ratio of the velocities in the slow and the fast directions.

Fitting this model to the graphene island morphology shown in **Figure 4.8.a** gives *r* = 0.25 ± 0.02. Notice such a large anisotropy in the model predicts that a sharp tip should develop at the apex of the lobe, as is indeed seen in **Figure 4.8.a**. Such sharp tips are evident on many of the lobes seen in **Figure 4.2.e**. The fitted anisotropy factor is approximately the same for many islands, as seen by the consistent ~2:1 aspect ratio of the lobes in **Figure 4.2.e**. This anisotropy also agrees with the direct measurements of the growth velocity shown in **Figure 4.8.b**. In fact, the model predicts growth velocities involved in determining island shape to within 6%. The validity of this simple model demonstrates that a two-fold-symmetric, angularly dependent growth velocity determines the distinctive shape of the lobes of polycrystalline graphene islands on Cu(100).

The two-fold symmetry of the growth velocity of individual graphene crystals on Cu(100) has interesting implications concerning the factors that influence it. If growth were dominated by either the graphene itself or the Cu(100) substrate, we would expect six- or four-fold symmetry, respectively. The observed two-fold velocity shows that the symmetries of both the Cu surface and graphene lattice influence growth. Because the growth velocity depends on the crystals of both materials it must also depend on their relative orientation. Graphene occupies a range of orientations relative to the Cu surface, a detailed analysis of which is included in Chapter 5.1. As previously shown in **Figure 4.2.e**, the long axes of the graphene lobes are most often aligned along Cu<001> in-plane directions. These directions do not correspond with any of the high-symmetry direction of the graphene in its *average* relative orientation.
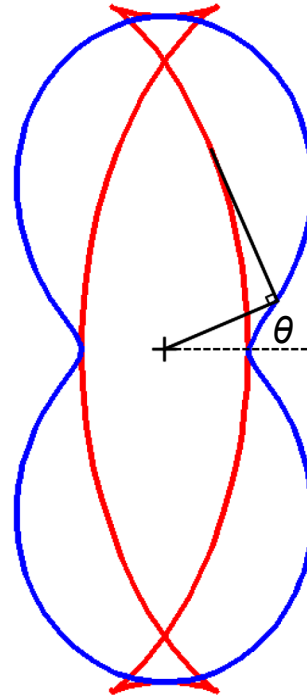
Figure 4.6 A schematic of a variation of the Wulff construction, with the a simple angularly dependent growth rate (blue, **Equation 1**) substituted for the surface anisotropy. Following the Wulff formalism allows the extraction of a steady-state growth shape (red, anisotropy factor *r* = 0.25).

(a) - Zigzag
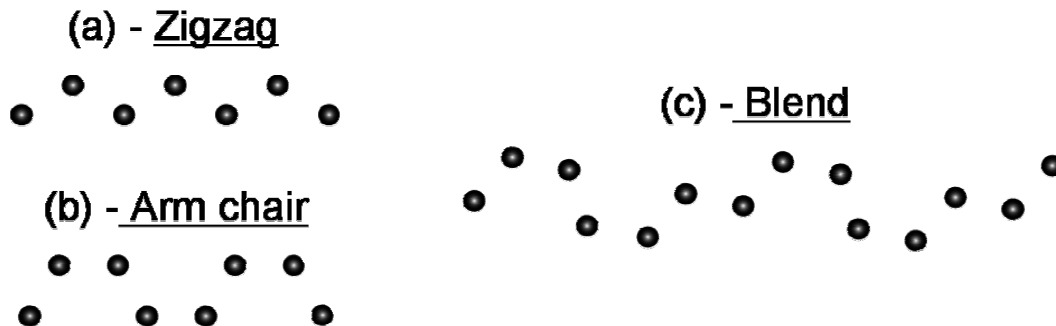
(b) - Arm chair

(c) - Blend

Figure 4.7 Schematic representations of the high-symmetry edge terminations of graphene, the zigzag (**a**), and armchair (**b**). Interestingly, the fast growth direction of graphene is along neither of these but rather a blended edge termination (**c**).

Instead, the graphene tends to be rotated 15° on average from alignment with Cu<001> directions. This yields a sheet whose fast-growing edge is approximately half way in-between the high-symmetry "zigzag" and "armchair" edge structures (**Figure 4.7.a-c**).

Orientation is not the only factor determining the velocity of the growth front. Growth rates are also affected by inhomogeneities on the surface. As the growth front intersects pinning sites or approaches an adjacent graphene island, its trajectory may be deflected from that predicted from the angularly dependent growth velocity. Additionally, while single Cu step edges do not have a perceptible effect on the growth, large bunches are observed to distort island evolution by altering growth trajectories (see yellow arrow in **Figure 4.2.e**). These effects may account for the significant lobe-to-lobe variations from the average orientation discussed above. For example, the fast growth direction is not always precisely along a Cu<001> direction. The non-90° angles between some lobes in **Figure 4.2.e** show it may be as many as 20° away.
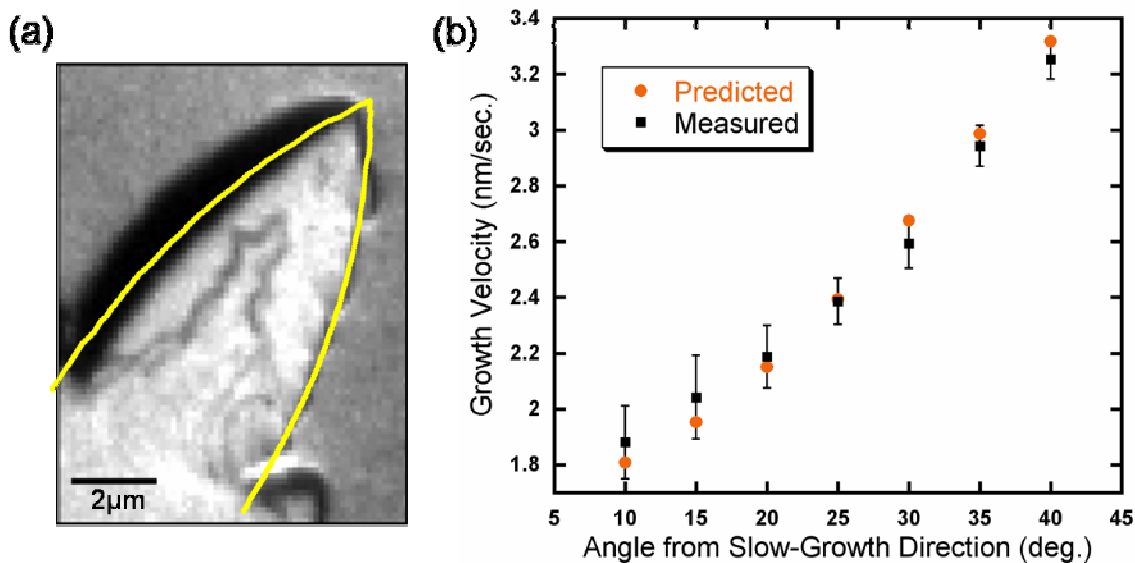
Figure 4.8 The profile of this graphene lobe (**a**) is well explained by the proposed two-fold symmetric growth velocity with an anisotropy factor of 0.25 (yellow line is the model fit). Furthermore, direct comparisons of the measured and predicted growth velocities (**b**) also show good agreement (anisotropy factor again 0.25).

The origins of the angularly dependent growth rate of individual graphene crystals on Cu(100) are thus far unclear. Previous work has shown that carbon monomers diffusing on a metal surface can face a large energetic barrier for attachment to graphene [33, 34]. This barrier may depend sensitively on the specific atomic geometry at the growth front, such as perhaps the relative positions of the graphene and the monomer surface binding site. Alternatively, if the graphene *edge* is strongly bound to the Cu substrate, attachment of monomers would require locally detaching the edge from the substrate. This would also create a barrier that would depend on the details of the configuration of the graphene edge. There is also a possibility that the nano-scale moiré, or superstructure, formed by the graphene-Cu(100) heterostructure plays a significant role (see Chapter 5.2). Regardless of its underlying causes, the anisotropic growth rate of graphene on Cu(100) dominates the morphological evolution of the film.

4.2.2 Diffusion limited growth – Au(111), Cu(111)

Graphene island growth on the (111) surface of Au or Cu is very different than on Cu(100). Rather than the evolution of island shapes being determined by the attachment kinetics of C at the graphene growth front, it is instead dictated by the influence of C diffusion on the surface of the substrate. The result of this is that graphene islands on Au(111) and Cu(111) form dendritic shapes. Dendritic crystal growth occurs when a flat crystal facet is unstable with respect to geometric perturbations. When a bump or protrusion develops on one of these surfaces it extends into a region with a higher concentration of C. This leads to positive feedback; the larger the perturbation becomes the higher the concentration it is exposed to. The same process may occur for an existing corner of a graphene island without the interruption of a flat face being involved. Island corners protrude into regions of higher concentration, and thus may undergo more rapid growth. The stages of graphene film growth on Au(111) observed here are purely dendritic.

Graphene islands on Au(111) are already heavily ramified when they reach sufficient size to be observable by LEEM. If allowed to grow uninterrupted by Au step bunches, those islands which nucleate homogeneously form roughly symmetric, six-branch snow-flake like shapes (see yellow arrow in **Figure 4.9.a**). Islands which nucleate heterogeneously, or which overlap Au steps during growth, develop a different morphology (see red arrow in **Figure 4.9.a**). These graphene islands grow much more rapidly parallel along the Au steps leading to an elongated island shape. Although the graphene islands expand more rapidly parallel to the Au steps the islands also grow perpendicular to them. Dendrite branches form which extend off from the main body of the island (see blue arrow in **Figure 4.9.a**). Why graphene tends to grow more quickly along step edges on the Au(111) surface remains unclear. Substrate steps have been shown to act as barriers to the diffusion of surface adatoms during growth [55, 56]. Substrate step edges can also attract adatoms, holding them in anisotropic traps and leading to local regions of high adatom concentration along their length [57]. Either of these phenomena could result in locally accelerated graphene growth. Rather than their influence on surface diffusion, it could be the interaction between the Au steps and the graphene itself that leads to accelerated growth. In some systems substrate steps have been shown to induce anisotropic graphene growth due to bonding between the steps and C film [13]. Clusters of steps on Cu(111) may similarly interrupt graphene growth by stimulating the nucleation of a differently oriented graphene domain, as will be discussed in the next section [58]. A slightly stronger interaction between the graphene and Au(111) steps could also account for the observed accelerated growth.

The extent and small size of the dendritic branching observed in graphene islands on Au(111) is indicative of a very short C diffusion length. For these island shapes to develop, the diffusion distance must be even smaller than the islands themselves. A contributing factor to the limited surface diffusion of C on Au(111) may be the characteristic "herringbone" surface reconstruction of the substrate [59] (this is discussed in depth in Chapter 6.3). Because the Au atoms on the surface of the crystal have a higher density than in the bulk it would not be unreasonable to expect the low-energy
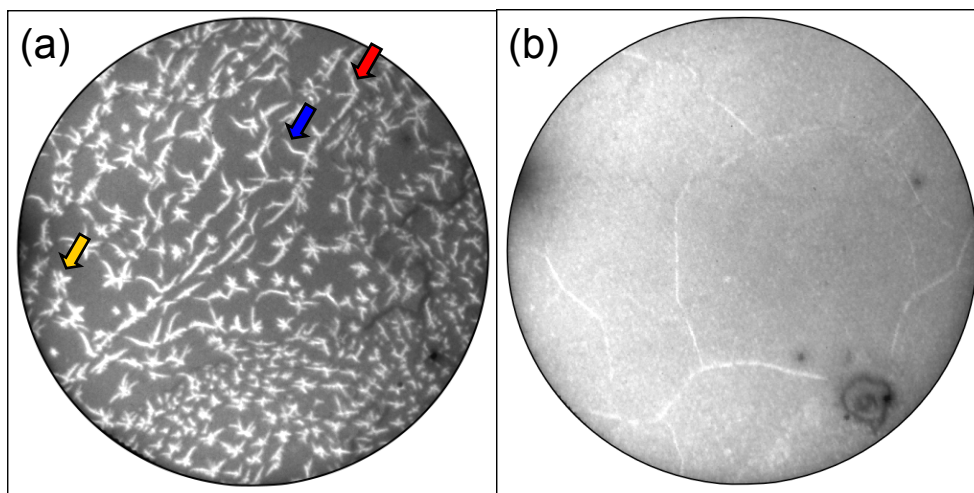
Figure 4.9 LEEM micrographs of graphene islands (**a**) and a full graphene film (**b**) grown on Au(111). Notice the highly ramified shape of the dendritic graphene islands in **a** (FOV = 9 μm). Islands which nucleate on Au steps (red arrow) grow more rapidly parallel to those steps, leading to elongated island shapes, and ribbons of continuous graphene along Au steps prior to full film formation. Branches also form on these islands which extend away from the Au steps (blue arrow). Islands on terraces (yellow arrow) form more compact, 6-fold symmetric dendritic shapes. No evidence of additional C accumulation is observed after the formation of a complete film (**b**) (FOV = 20 μm). Notice the wrinkles which have formed due to the difference in coefficient of thermal expansion between the two materials.

configuration of a C monomer to be influenced. An unconventional equilibrium position for C monomers on Au(111) would have a corresponding impact on their diffusion. However this remains speculative, and the origin of the highly ramified graphene islands observed here remains an open question.

Even when concentration gradients exist on a substrate surface dendritic growth does not always occur, as is the case for graphene on Cu(111). Highly anisotropic surface energies may provide sufficient energetic benefit to maintaining smooth crystal facets that dendrite formation is inhibited. Significant surface or edge diffusion along the perimeter of the crystal has a similar effect. Crystal growth in an environment which supports concentration gradients represents a balance between the factors stabilizing crystal facets, and dendrite formation. This balance may shift during a growth process. For instance, the size of the growing islands relative to the average diffusion length on the surface may change. It is thus possible to move from a growth regime where surface energy anisotropy and edge diffusion dominate to one where concentration gradients on the surface are instead the determining factor. This transition is indeed observed in graphene growing on Cu(111) as the size of the islands increases.

Although graphene islands growing on Cu(111) may also form dendritic shapes this system has additional complexity. Graphene islands are generally still compact when they reach a large enough size to be visible in LEEM. Many of these islands also have extended flat sections on their perimeter which are often separated by 60° angles. Because these flat sections reflect the symmetry of the C crystal they are likely well defined crystallographic facets. A graphene island at this stage of growth is shown in **Figure 4.10.c**. Once the graphene islands reach a critical size they loose their regular shape and begin to form dendrites. The island size at which this transition occurs varies
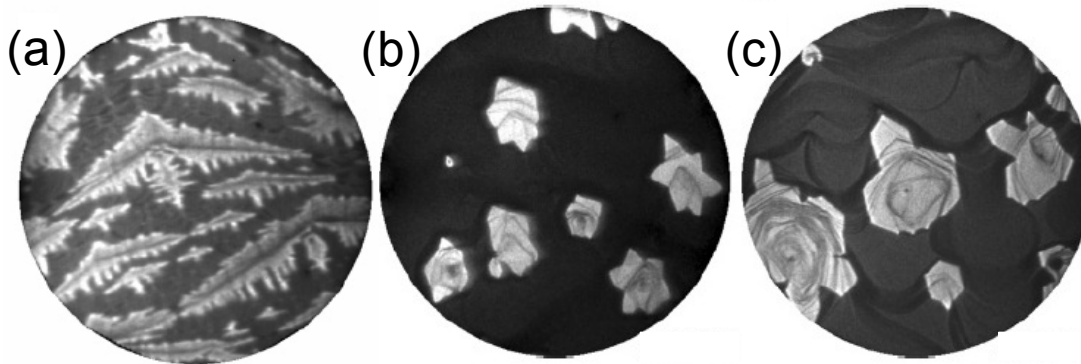
Figure 4.10 LEEM micrographs of graphene growing on Cu(111) at 690 ºC (**a**), 950 ºC (**b**), and 975 ºC (**c**) showing the difference in island sizes ramification starts to occur due to dendritic growth. This emphasizes the temperature dependence of C diffusion on Cu(111) over the temperature range appropriate for graphene growth (FOVs are **a** = 7 μm, **b** = 20 μm, and **c** = 14.5 μm).

considerably over the range of growth temperatures suitable for graphene synthesis. At 690 ºC the graphene islands are dendritic almost immediately (**Figure 4.10.a**), resembling the growth behavior on Au(111). At higher growth temperatures, say 950 or 975 ºC, the islands are capable of reaching over 5 μm in lateral dimension prior to the onset of dendrite formation (**Figure 4.10.b**, **c**).

The temperature dependence of the onset of dendrite formation for graphene islands on Cu(111) is likely due to the variation in the diffusion length of C on the substrate. Because diffusion is a thermally activated process, low growth temperatures lead to shorter diffusion distances. The shorter the diffusion distance the steeper the gradients in adatom concentration which may be supported. Thus, compact island shapes become unstable at smaller sizes. Higher growth temperatures cause the average distance over which a C adatom may diffuse to be significantly higher. This smoothes concentration gradients and leads to larger stable crystal sizes. The contrast between **Figures 4.10.a** and **.b** and **.c** dramatically illustrates this. It is also possible that the onset of dendritic growth is influenced by temperature driven changes in the free energy of the various graphene edge terminations. However, the dominance of adatom surface diffusion demonstrated in **Figure 4.11**, and the last paragraph of this section, makes this likely only a secondary effect.

The transition in the growth mode of graphene on Cu(111) from stable to dendritic shows that growth takes place near the intersection of these two paradigms. At the stage of island growth we inspect the crystal feature sizes and adatom diffusion length are similar in magnitude. Indeed, these two factors are close enough that the characteristic size of an island may overtake the diffusion length during the expansion of an individual island. For this reason we observe both stable and dendritic growth within the same experiment. It is also possible to control the transition between the two using the growth temperature. This gives the experimentalist an additional tool with which to probe the system.
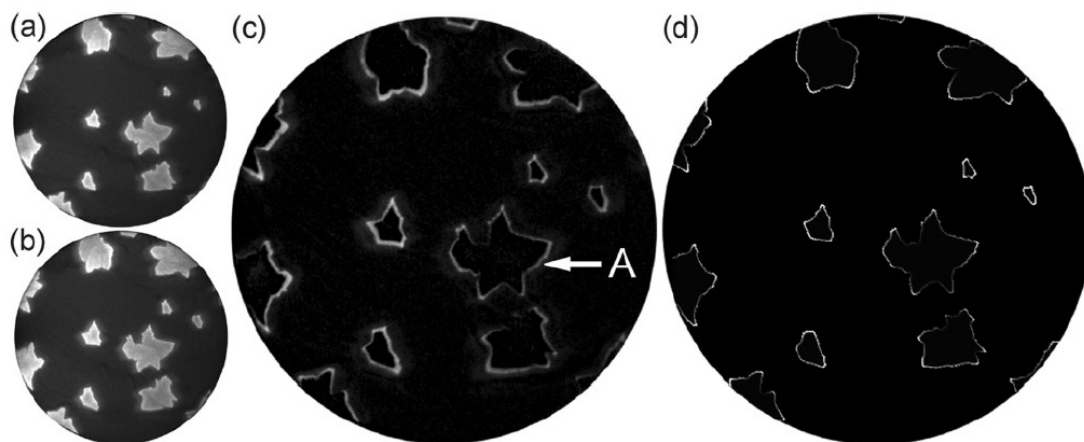
Figure 4.11 (**a**, **b**) LEEM micrographs separated by 61 seconds during graphene growth on Cu(111) at 893 C (FOV = 20 mμ). (**c**) Difference between **b** and **a**, where the bright strips show the incremental growth that occurred between image collection. (**d**) Flux to the edges as computed by solving the diffusion equation for a uniform deposition flux onto this particular surface geometry of graphene islands. The grayscale intensity is proportional to the flux to the island edges. The excellent agreement between **c** and **d** shows the powerful influence of surface diffusion on graphene growth on Cu(111). The author would like to acknowledge Dr. Norm Bartelt of Sandia National Laboratories.

It is possible to directly observe the diffusion dependence of graphene growth on Cu(111). This is done by comparing the observed graphene growth rate with an approximation of the adatom flux that particular segment of growth front experiences. The growth rate of the graphene is graphically extracted by subtracting two LEEM images separated by a brief time (**Figure 4.11**). The C adatom flux impinging on the perimeter of the islands was estimated by numerically solving the diffusion equation for the observed surface configuration. The method is similar to that used to evaluate secondary nucleation on Cu(111) (Section 4.1). The excellent agreement between the two shows that surface diffusion is the dominant factor in determining graphene island shapes in the later stages of growth. This result also points out that the specific distribution of graphene islands on the surface influences growth. Likewise, it is important to note that the compact shape of the graphene islands plays a role. Those portions of a graphene island that protrude along its perimeter are more likely to experience a high adatom flux. By this mechanism hexagonal, faceted islands may develop into six-lobed star shapes as the corners grow at an accelerated pace. **Figure 4.12** is a schematic illustrating this process. The surface diffusion of C adatom species is the controlling factor in the morphological evolution of graphene growing on the (111) surface of both Cu and Au.

Figure 4.12 A schematic showing how a faceted graphene island on Cu(111) may develop into a six-pointed star during growth. This is an example of how the shape of an island prior to dendrite formation may be significant.
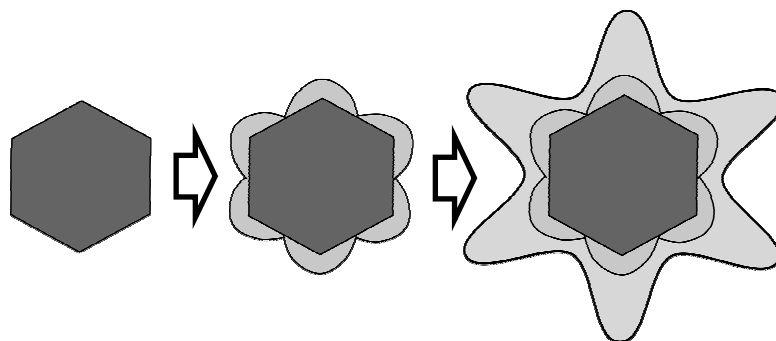
4.3 Domain distribution during growth

The range of growth behaviors demonstrated by graphene results in corresponding variations in the distribution of graphene crystalline domains. The constituent grains of a graphene film are differentiated from one another by a rotation about the film normal. Essentially, they form an extremely well ordered out-of-plane textured film. LEED shows these rotations quite clearly. The hexagonal diffraction pattern of graphene rotates around the specular beam depending on the orientation of that graphene domain. This is shown in **Figure 6.1** for graphene on Cu(111). The simplest scenario of the substrates examined here is graphene grown on Au(111). To within the spatial sensitivity of LEEM and selected-area LEED, each individual island is a single graphene domain which initiated growth from one nucleation site. In this case, the factors that determine graphene domain size are the nucleation density in combination with the degree of crystalline alignment between neighboring islands.

The distribution of domains in graphene grown on Cu(100) and Cu(111) is more complicated than on Au(111). Unlike those on Au(111), graphene islands growing on Cu(100) tend to be composed of multiple distinct domains. The internal crystalline structure of these islands is the result of an orientation selection process that unfolds soon after nucleation. The site of this process is market by a region of local relatively high crystalline disorder overlying the original nucleation point, which can be seen in **Figure 4.3**. The initially disordered growth allows graphene to sample all possible relative orientations between the two materials. When the growth front has adopted a preferential orientation it stabilizes and growth accelerates rapidly. The swiftly expanding domains quickly come to dominate the island structure. It is this process of settling into preferred relative orientations that leads to the distinct crystalline distribution within the four-lobed graphene islands on Cu(100).
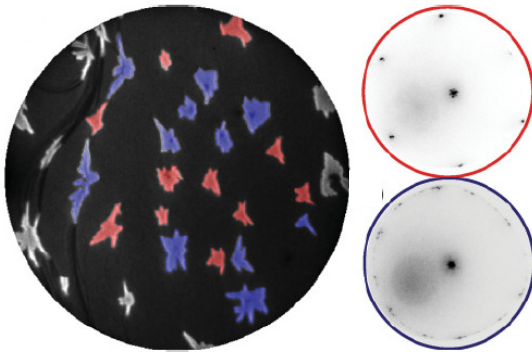
Figure 4.13 LEEM micrograph (**a**) of graphene islands growing on Cu(111) at 815 ºC (FOV = 14.5 μm). Red islands are single crystals, aligned within 4º of the Cu lattice (**b**), and mainly nucleated homogeneously after an abrupt increase in the C flux. Blue islands are polycrystalline (**c**), and generally nucleated heterogeneously. The author would like to acknowledge Dr. Shu Nie of Sandia National Laboratories.

A (111) oriented Cu substrate is also capable of inducing multi-domain graphene islands. Two distinct processes contribute to this. Similarly to growth on the (100) facet, graphene islands which nucleate heterogeneously on Cu(111) tend to be polycrystalline. These are also usually the first islands to grow. Islands that initiate growth through homogeneous nucleation are frequently composed of a single graphene domain. A comparison correlating LEEM and LEED in **Figure 4.13** illustrates this difference. Why heterogeneous nucleation induces polycrystalline islands remains unclear, but is perhaps due to surface features that interfere with the trajectory of the growth front. The orientation selection process
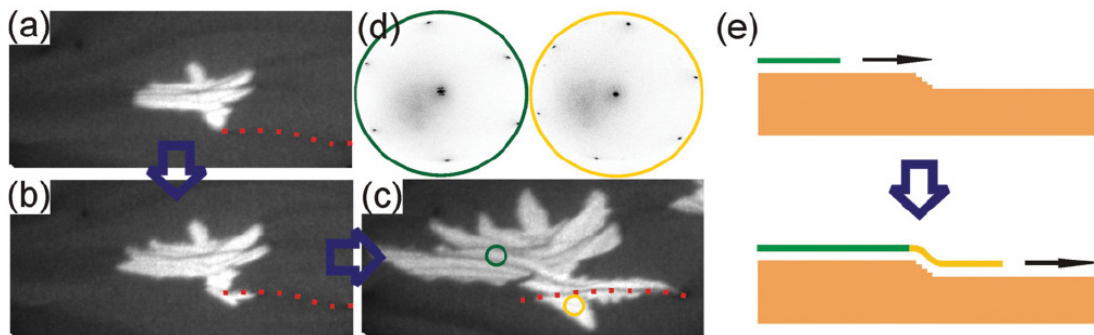
Figure 4.14 Sequence of LEEM images (**a-c**) showing a graphene island growing at 893 ºC (FOV = 9 x 4 μm). The dotted red line marks a Cu step bunch, with (**d**) LEED patterns taken from the graphene on either side. The rotation of the graphene upon growth over the step bunch is revealed by the rotation of the diffraction spots. (**e**) Schematic depiction of the change in C lattice orientation (green to yellow) that may arise when an island grows across such a step bunch. The author would like to acknowledge Dr. Shu Nie of Sandia National Laboratories.

which occurs on Cu(100) does not occur in symmetry matched epitaxy on the (111) surface under similar growth conditions. However, it is curious to note that crystalline disorder within graphene islands on both Cu(100) and Cu(111) is highly correlated with heterogeneous nucleation. In addition to heterogeneous nucleation a second mechanism contributes to multi-domain graphene islands on Cu(111). In this case graphene growth fronts have a propensity to crystallize new material with a different lattice rotation as they move across large Cu step clusters. This process is illustrated in **Figure 4.14**. Graphene islands have fundamentally different distributions of constituent domains on Cu(100), Cu(111), and Au(111). The diverse processes that lead to these distributions illustrate how the manner in which graphene growth proceeds may dramatically affects the structure of the resulting film.

4.4 Mobile substrate step edges during growth

Elevated substrate temperatures are required to yield C films composed of well ordered graphene. These temperatures are sufficient to induce the metal substrates examined to simultaneously evaporate during C deposition. The result of this evaporation is a dynamic, constantly evolving growth surface characterized by mobile substrate steps. Growing graphene interacts with these mobile step edges differently depending on the substrate in question. As discussed previously, graphene grows more rapidly along steps and step bunches on Au(111), as shown in **Figure 4.9.a**. It is interesting that mobile Au steps are also capable of flowing completely beneath established graphene islands without noticeably influencing their growth. Substrate steps on Cu(111) play a more nuanced role during graphene growth. Cu(111) step edges may serve as heterogeneous nucleation sites in the early stages of C deposition. Occasionally a graphene island nucleates at the point such that it overgrows the intersection of a screw dislocation with the Cu(111) surface. This causes the graphene island to grow above a spiral of Cu steps, as is shown in **Figure 4.15**. The most significant influence substrate steps have during graphene growth on Cu(111) is stimulating the formation of new C

domains. It is curious to note that unlike Cu(100), steps on the (111) facet do not generally accumulate beneath the graphene islands.

Figure 4.15 A graphene island on Cu(111) which nucleated where a screw dislocation intersected the substrate surface (FOV = 14.5 μm).

The morphological evolution of the Cu(100) substrate surface during graphene growth is more dramatic than that of either (111) oriented crystals. The step edges on Cu(100) interact with pinning sites, grain boundaries, and the growing graphene itself. This yields a constantly changing surface. Prior to C deposition, the surface of each Cu grain consists of a propagating array of monolayer height steps. After growth large Cu hillocks have developed underneath the graphene islands, as is shown in **Figure 4.16.a**. The schematic in **Figure 4.16.b** sketches the process by which the hillocks form. When a segment of a Cu step edge collides with a graphene island, it decelerates. This leads the Cu steps to stack up on one another, and become bunched under the graphene. The deceleration of the Cu steps is likely due to the necessity for Cu atoms to diffuse laterally in order to sublime. A Cu atom must move from underneath a graphene island onto the exposed Cu surface before evaporating. Because the step bunches move slowly beneath the graphene, they are unable to flow through the island before being impinged upon by additional Cu steps. As a consequence incoming steps wrap around under the
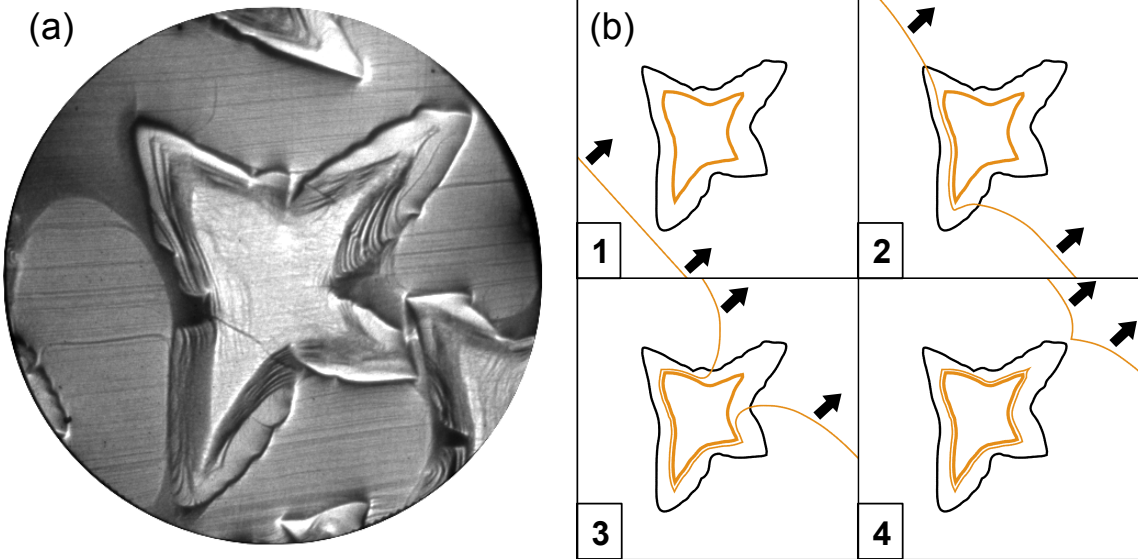
Figure 4.16 LEEM micrograph of a graphene island on Cu(100) (**a**) with the step edges comprising a pronounced Cu hillock easily visible within the interior of the island. (**b**) A schematic showing the hillock formation process which occurs during growth. Interestingly, the Cu steps do not significantly alter the growth behavior of the graphene, unlike those on Cu(111) substrates.

interior of the lobed graphene island. Each wrapped step lowers the adjacent bare Cu by an atomic step spacing relative to the graphene covered region. This process creates Cu hillocks which mirror the four-lobed shape of the graphene draped across them. The hillocks become more prominent with increasing growth temperature. This is because the additional step flow leads to more of the associated step looping. The raised sections of Cu may be so dramatic as to be easily visible by optical microscopy. As the graphene islands coalesce, Cu step flow is increasingly inhibited. Because of these step-to-graphene interactions, vapor pressure must be a consideration when evaluating the utility of substrates for graphene growth.

It is interesting to note that step edges and step edge bunches do not stimulate the nucleation of new graphene orientations on Cu(100). This is a particularly tangible example of the differences in interaction between graphene and Cu(111) or Cu(100). It points to a fundamental difference where step edges on the (100) surface do not interact with graphene as strongly. Although they accumulate beneath the graphene islands, steps cause very little observable disruption to the growing C film. Conversely, this emphasizes the fact that step edges on Cu(111) bond with the graphene film sufficiently to alter its growth behavior. Differences in the role of step edges on Cu(111) and Cu(100) show the variety of ways substrate symmetry influences graphene growth.

4.5 Monolayer films

The experiments presented here show that all three substrates examined support the growth of predominantly monolayer graphene films. As mentioned previously, this property of Cu foils has been attributed to the low solubility of C through sequential isotope labeling during CVD growth [41]. This finding was further confirmed by monitoring graphene films of approximately 0.5 monolayer coverage during cooling from the growth temperature (**Figure 4.17**). By continuously imaging the graphene-Cu(100)
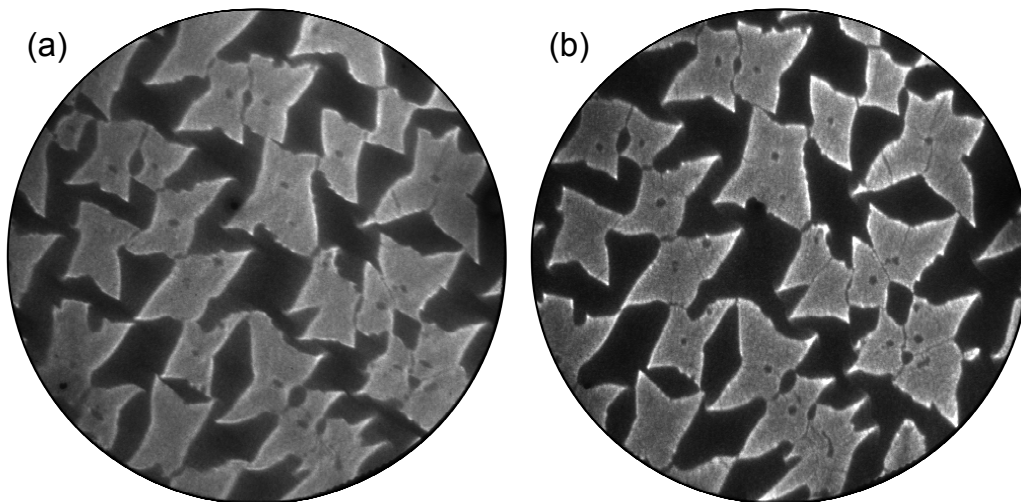
Figure 4.17 LEEM micrographs of graphene islands on Cu(100) after the halt of C deposition at 776 ℃ (**a**), and the same region of the sample surface after cooling to ~60 ℃ (**b**). No increase in island size could be detected during cooling. This shows that little C dissolved into the substrate during graphene growth (FOV = 20 μm).
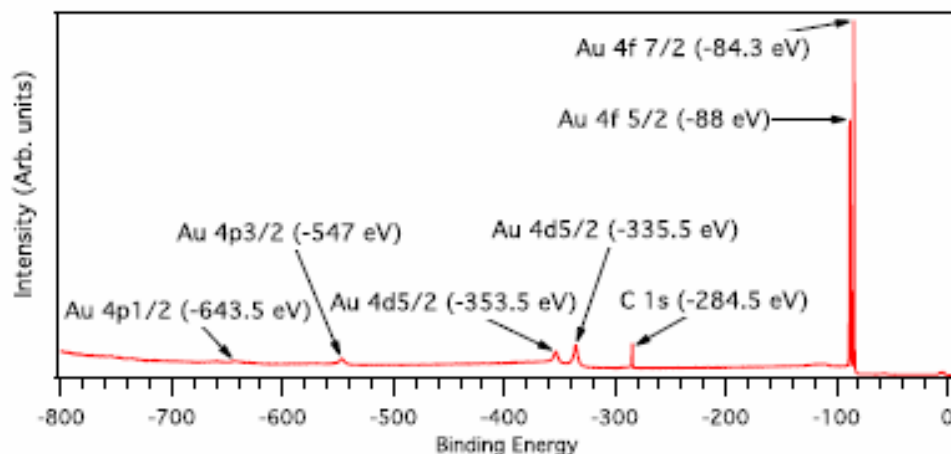
Figure 4.18 X-ray photoelectron spectroscopy collected from graphene on Au(111) showing only Au and a single species of C present. This eliminates the possibility of surface contaminants or other C species. Taken at a photon energy of 900 eV. The author would like to acknowledge Dr. Andrew Walter.

with LEEM any increase in surface coverage could be identified. As **Figure 4.17** shows, no island growth was observed during cooling. Additional checks for precipitated C were made by X-ray photoemission spectroscopy (XPS) on a partial graphene film on Au(111) (**Figure 4.18**). This is important because precipitated C might be amorphous and thus not generate sufficient contrast to be visible in LEEM. Only the XPS signatures of Au and graphene were observed, eliminating the possibility any other C phase being present.

The quantity of C on the surface was also limited by the lack of further accumulation on top of the first graphene monolayer. Even with continued exposure to the C flux only one graphene layer was ever observed to form. There are multiple possible explanations for this. Elemental C may have a low sticking coefficient on pristine graphene at the growth temperatures used. Alternatively, nucleating a new crystal on a graphene surface may require a much larger critical nucleus size than on metallic substrates. This possibility is supported by the observation that when a second graphene layer does nucleate on Cu foils, it generally does so at the same location as an earlier island [41]. The heterogeneity which stimulated the initial nucleation protrudes through the film. It should be noted that the experiments performed here include only a portion of possible growth conditions. Additional accumulation of C on the surface is surely possible with a sufficiently high flux.

4.6 Wrinkle formation during sample cooling

We observe the formation of wrinkles in graphene films while they are cooled from the growth temperature. This phenomena is widely reported in the literature [35, 43]. The wrinkles are linear, elevated regions in which the graphene film has delaminated from the metal substrate. Strain induced from the difference in coefficient of thermal expansion between the substrate and C film drives their formation. An example LEEM micrograph of wrinkled graphene on Au(111) is shown in **Figure 4.9.b**. Cu and Au contract with linear expansion coefficients of 18.3×10^{-6} K^{-1} and 15.8×10^{-6} K^{-1},

respectively [60]. The extent of wrinkle formation is a balance between thermally induced strain and the bond strength between the graphene and metal surface. The graphene wrinkles form a random matrix, with no apparent dependence on the crystallinity of the surface. Wrinkles in the graphene film again points out the unique features of two-dimensional epitaxy. Because the graphene film is only a single monolayer thick it is capable or relaxing the thermal strain by deforming in the out-of-plane direction. This avenue for strain relaxation is generally not available in traditional thin-film epitaxy. Thermal strain driven wrinkle formation is an inherent feature of graphene growth on Cu and Au.

Chapter 5 Graphene Film Microstructure

The microstructure of a polycrystalline graphene film is determined by the size of its constituent domains and the relative orientation of their crystalline lattices.   The substrates examined in this study each have a different orientational relationship with the graphene domains on their surface, resulting in corresponding microstructural variations in the films. Graphene may adopt a range of different configurations on a metal surface, with each configuration defined by the relative angle of the two crystal lattices. Rotational variability is a primary source of crystalline disorder in graphene films grown on metals. Establishing control over this degree of freedom is crucial to improving film quality.   Both LEED and ARPES were used to measure the relative orientation of graphene domains.   Domain size within a polycrystalline graphene film is another important influence on its overall properties.   Grain boundaries are required to stitch together the constituent grains of a polycrystalline graphene film.   Thus, the size of the domains is the determining factor of the total line length of grain boundaries.   This is an important consideration because grain boundaries may act as scattering centers for both charge carriers and phonons [61, 62].   Each substrate examined here produced a different distribution of grain sizes. Furthermore, the growth characteristic which determined the domain size was also variable.   In the case of films grown on either Cu orientation, the nucleation density and mosaicity of islands dictate the size of the graphene domains. On Au(111) the exceptional rotational ordering of the C crystals leads to a more complicated situation.   The microstructures varies considerably between graphene films synthesized on Cu(100), Cu(111), and Au(111) substrates.
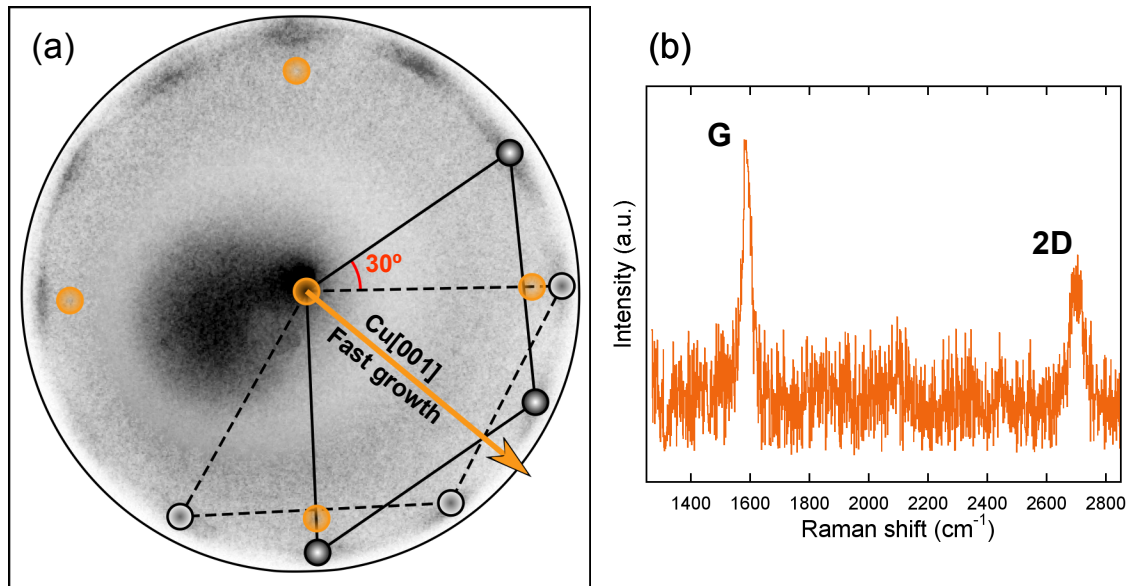
Figure 5.1 (**a**) LEED from a large region of a graphene film grown on Cu(100). Because the illuminated region of the sample contains graphene of many different relative orientations the pattern is diffuse, but represents a statistical sampling of the surface configuration. Notice the twelve arcs, each spanning $\sim\pm9°$, which are centered on the two crystallographically equivalent aligned configurations of six-fold symmetric graphene on the four-fold symmetric surface. The existence of two degenerate configurations, combined with the spread within each, results in significant crystalline disorder. Raman spectroscopy of graphene on Cu(001) (**b**) does not show any peak shifting from their position in unstrained graphene, suggesting there is little strain in the film.

Graphene films grown on Cu(100) contain substantial rotational disorder. A portion of this variability is due to the symmetry mismatch between the two materials. The combination of the six-fold symmetric C film and four-fold symmetric Cu substrate results in two crystallographically equivalent orientations the graphene may occupy. A LEED representation of these two orientations is shown in **Figure 5.1.a**. Because the two orientations are degenerate, the graphene domains are evenly split between them. For this reason graphene films grown on Cu(100) will always contain a certain unavoidable level of crystalline disorder. However, as **Figure 5.1.a** shows the graphene does not occupy only these two exact orientations. Instead there is substantial scatter around each symmetry-defined orientation; the most common graphene rotations are within ~±9° of aligned. Due to the crystallographic dependence of the graphene growth rate on Cu(100), it's rotational distribution is coupled with it's kinetically dominated growth behavior.

Graphene grown on the symmetry matched (111) surface of Cu has a much higher degree of orientational ordering than is produced by Cu(100). The majority of graphene domains on Cu(111) adopt orientations within ±3° of aligned with the Cu surface. This is illustrated in the composite dark-field LEEM map in **Figure 5.2**. We define aligned as
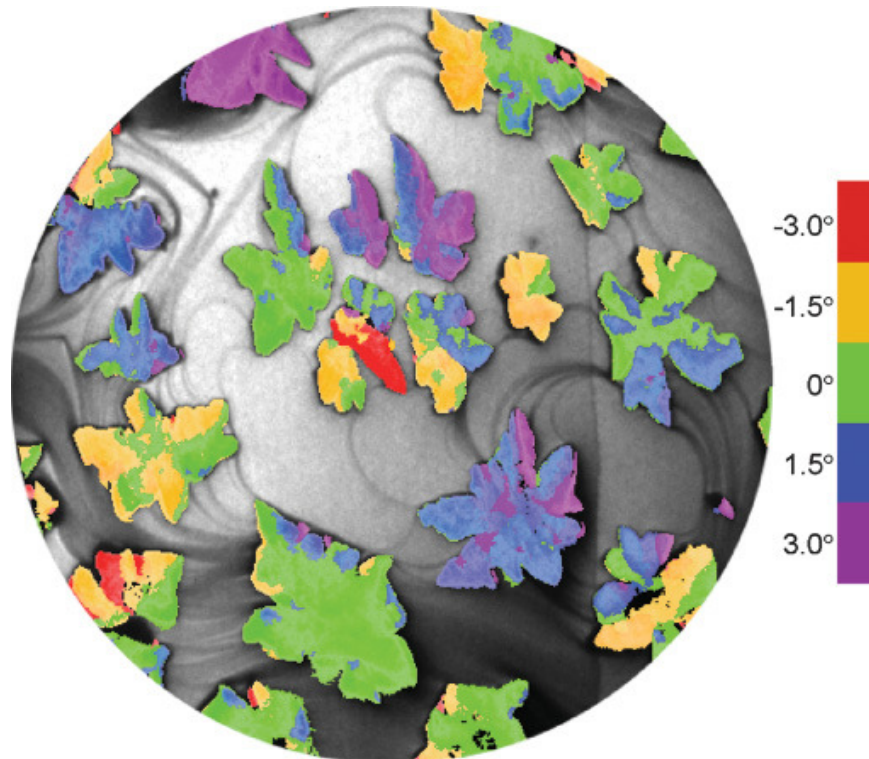
Figure 5.2 A dark-field LEEM analysis of graphene grown on Cu(111) at 900 ºC. The image is a composite of five dark-field micrographs obtained in 1.5º rotational increments from the Cu[11$\bar{2}$] direction at 0º. The saturation of each color reflects the degree graphene is aligned to each angle. The majority of graphene domains grown on the (111) facet of Cu adopt an orientation within 3º of aligned with the substrate (FOV = 10 μm). The author would like to acknowledge Dr. Shu Nie of Sandia National Laboratories.

when the C[01] and Cu[1 Ī 0] directions are parallel. The increase in orientational homogeneity in graphene films grown on Cu(111) may be partially attributable to the low lattice mismatch between the two materials. Graphene's lattice parameter of 2.46 Å is only ~3% smaller than the 2.56 Å Cu(111) surface lattice parameter. Interestingly, the rotational deviation of a graphene island on Cu(111) is heavily influenced by how that island nucleated. Graphene islands which nucleate heterogeneously generally show misalignment with the substrate surface. Those islands which nucleate homogeneously, usually later in growth, tend to have their lattices very closely aligned with the Cu(111). This dependence is illustrated in **Figure 4.13** in Chapter 4. Homogeneous graphene nucleation on Cu(111) is stimulated by a locally high C adatom concentration. Because of this, a kinetic pathway to the lowest energy configuration is open. Those islands that form heterogeneously preserve some remnant of the surface defect which stimulated nucleation as they propagate. From this comparison we are able to infer that the preferred configuration of graphene on Cu(111) is precise alignment with the substrate. Improvements in graphene growth on Cu(111) may be achieved by using substrates with exceptional surface quality. This will inhibit heterogeneous nucleation and reduce the associated rotational disorder.

The development of distinct crystallographic domains in graphene films grown on Cu(100) and Cu(111) reflects the growth behavior previously discussed. Graphene's in-plane orientational variation on the Cu substrates is such that individual islands remain physically distinct after they are incorporated into a complete film. The same is usually true for intra-island domains. This means the size individual graphene islands reach prior to coalescence is the limiting factor in determining domain size in a graphene film, be the island comprised of a single or multiple domains. The inherent polycrystallinity of graphene islands growing on Cu(100) means that the size the island lobes reach determines the domain size in the final film. The experiments conducted here showed graphene island lobes reached approximately 15 μm across prior to inter-island impingement, corresponding with reports in the literature [39, 63]. On Cu(111) graphene islands reached 10-15 μm in lateral dimension prior to inter-island impingement. This leads to a similar average domain size to films grown on Cu(100). It would be advantageous to allow graphene island growing on Cu(100) and Cu(111) to reach a larger size prior to incorporation into a complete film..

One strategy to increase the size of domains within graphene films grown on Cu(100) and Cu(111) is to reduce the nucleation density of islands. Surface quality is an important factor in nucleation density on these substrates. Recent reports have shown that individual islands hundreds of μm across may be grown on Cu(100) by depressing the nucleation density of graphene [64]. This is accomplished by folding the Cu foil substrate into an envelope prior to the deposition of C by CVD. It is probable that the Cu vapor pressure inside the envelope limits substrate step flow, allowing for uninterrupted graphene growth. Although the crystalline composition of these enormous islands has not been definitively established, it is certainly possible they contain correspondingly large crystalline domains. A second strategy which has been developed is to manipulate graphene nucleation by deliberately seeding it at pre-patterned sites on the substrate [65]. Further research is needed to judge the advantages this may offer. In general, careful

surface preparation of Cu substrates will lead to larger graphene domains by reduced heterogeneous nucleation, and an overall lower nucleation rate. The similar microstructure of graphene grown on Cu(100) and Cu(111) falls short of the degree of organization achieved by graphene on Au(111).

Graphene grown on Au(111) shows a remarkable degree of epitaxial fidelity with the substrate. LEED analysis reveals that there is a single, dominant, in-plane graphene orientation relative to the Au(111) single crystal substrate. Moreover, in this orientation the lattices of the graphene and Au(111) are aligned (C[01] and Au[1-10] are parallel). An example LEED pattern from a graphene domain on Au(111) oriented in this way is shown in **Figure 5.3.a**. We label this orientation R0, as illustrated in **Figure 5.3.c**. Small fractions of the graphene film are rotated by 30º relative to the Au lattice, which we label R30 (**Figure 5.3.d**), or are randomly oriented. The high degree of orientational homogeneity in these films contrasts with graphene grown on Au(111) by a modified CVD process, which displays extensive rotational disorder [66]. Not only is there an even distribution between the R0 and R30 orientations, but there is also significant variation of alignment within each of these configurations. The two sets of diffraction arcs generated by the distribution of relative orientations in the CVD films are comparable to those resulting from the scatter around graphene's two degenerate configurations on Cu(100) (**Figure 5.1.a**). From the perspective of classical thin-film epitaxy, it is puzzling that the R0 orientation is the most prevalent due to its substantially higher lattice mismatch of ~17% compared to the relatively modest ~1.5% mismatch for R30 graphene. Indeed, it is for this reason that the R30 orientation has generally been examined in theoretical studies [67, 68] and considered to be the more stable epitaxial orientation [69].

The dominance of the R0 orientation is striking. The LEEM micrographs in **Figure 5.4.a-d** demonstrate this. The sub-monolayer graphene coverage displayed in these images conveniently allows for contrast between the islands and remaining exposed Au substrate. Furthermore, the set of over 450 individual graphene islands in these
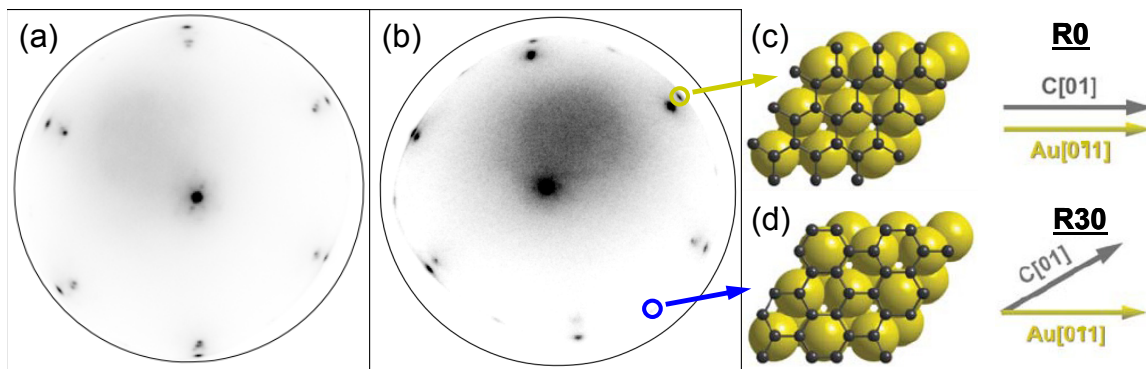
Figure 5.3 LEED from a single R0 oriented graphene domain on Au(111) (**a**) and from a larger region of the surface (**b**) which simultaneously samples many different graphene domains including both R0 and R30 regions. Notice from the relative intensities in **b** that the vast majority of graphene occupies an R0 orientation, as is schematically shown in **c**, while a small minority adopts a 30º degree rotated orientation (**d**). As the schematics in **c** and **d** show, each orientation results in a substantially different local configuration of atoms.

particular images offer a thorough statistical sampling of the range of graphene-Au(111) orientations. Comparison between the bright-field (**Figure 5.4.a,c**) and dark-field (**Figure 5.4.b,d**) LEEM images shows that over 95% of graphene islands have the R0 orientation. The underlying mechanisms which induce this degree of ordering are difficult to unambiguously identify at this time.

Using angle-resolved photoemission spectroscopy, we have mapped the electronic structure of epitaxial graphene on Au(111). The resulting Fermi surface, as shown in **Figure 5.5.a**, confirms the distribution of graphene orientations identified by LEED. The ARPES spectra in **Figure 5.5** have low background signals and narrow line widths. As the line width of ARPES spectra are directly related to the defect scattering rate, this indicates a clean, well-ordered graphene layer. The Fermi surface also shows few states that are not attributable to R0 or R30 graphene. This further demonstrates the structural homogeneity of the sample. Graphene's characteristic linear electronic dispersion is unmistakable in the band structure plots along the Γ-K direction. The dispersion is
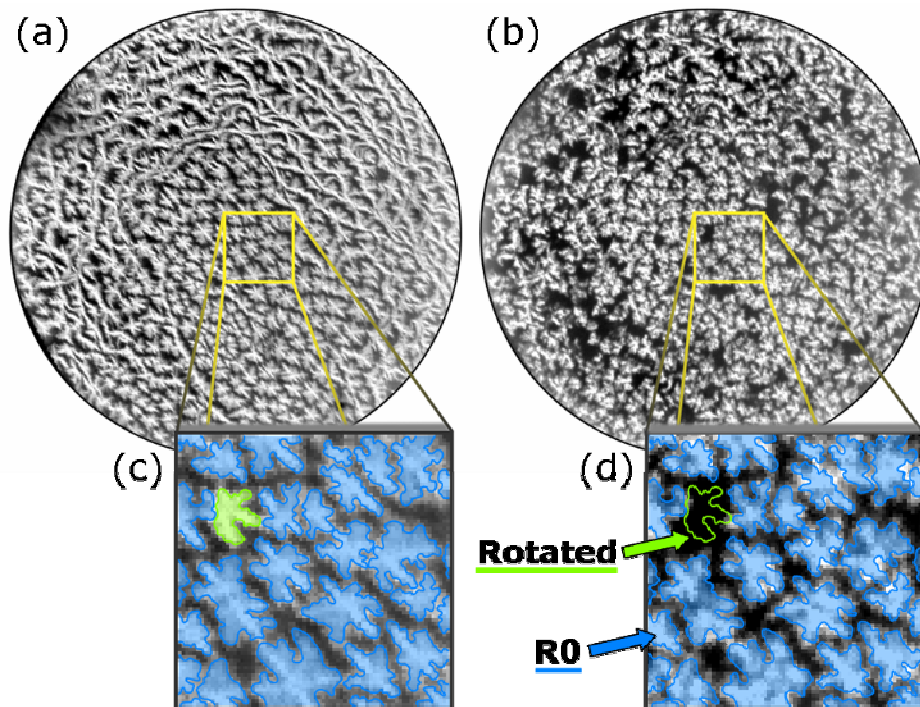
Figure 5.4 **(a)** Bright-field LEEM micrograph of approximately 0.75 monolayers of graphene on Au(111) grown at 880 ℃, and a dark-field micrograph **(b)** of the same region of the sample surface taken in the first order diffraction condition of the R0 orientation of graphene. Islands with the R0 orientation will be visible in both **(a)** and **(b)**, while those with any other orientation will be illuminated in **(a)** but will generate no contrast in **(b)**. This distinction is demonstrated in the expanded bright-field region **(c)** and dark-field region **(d)**. R0 oriented islands, outlined and tinted blue, are bright in both **(c)** and **(d)**, while the single island of a different orientation within this region, outlined and tinted green, is bright only in **(c)**. Over 95% of islands have the R0 orientation, resulting in a quasi-single crystal film upon their coalescence. The field of view is 9 μm for **(a)**, **(b)**, and 1.2 μm for **(c)**, **(d)**.
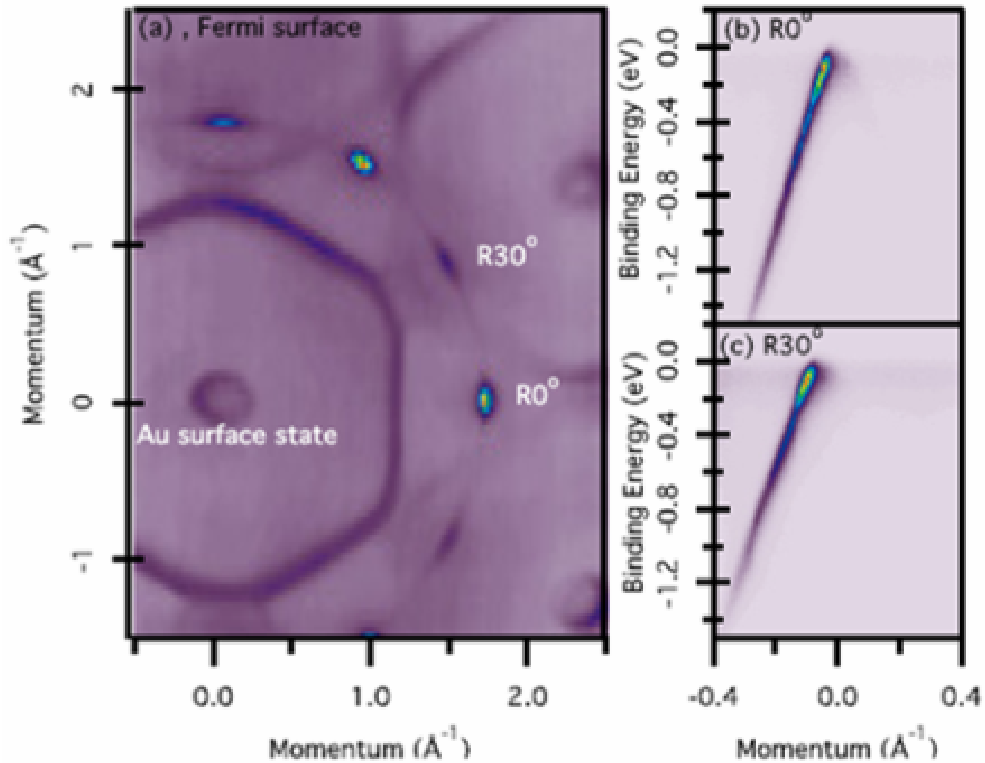
Figure 5.5 ARPES Fermi surface and band-structure maps of graphene on Au(111). The Fermi surface distribution in **a** shows the dominance of the R0 orientation with a small fraction of graphene domains at R30, leading to a quasi-single crystal film. Charge transfer with the Au substrate lowers the graphene Fermi level, resulting in a slight *p*-type doping with a concentration of ~6.2x10^{11} holes/cm^2. Notice the persistence of the Au surface state indicative of a clean Au surface. Spectra along Γ-K for the R0 (**b**) and R30 (**c**) orientations show that both maintain the characteristic linear dispersion of free-standing graphene. The author would like to acknowledge Dr. Andrew Walter.

extremely close to that of free-standing, high-quality graphene with no evidence of defect induced deterioration (**Figure 5.5.b**,**c**). Interestingly, the linear dispersion near the charge neutrality point is preserved for both R0 and R30 orientations along their respective Γ-K directions, despite the fact that there is a substantially different local configuration of C atoms relative to the underlying Au (**Figure 5.5.b**,**c**, **Figure 5.3.c**,**d**). The structure of the Fermi surface and preservation of graphene's linear dispersion are both indicative of a graphene film of high crystalline quality that is decoupled from the Au substrate. This weak coupling between graphene and Au is consistent with theoretical calculations [69] as well as experimental investigations of Au-intercalated graphene [70-72].

Graphene films supported by metal substrates generally display charge transfer with the metal surface and both the R0 and R30 orientations on Au(111) are no exception (**Table 5.1**). The Fermi level shift superimposed on the high-quality, defect-free ARPES spectrum of graphene on Au(111) is the most noteworthy evidence of the interaction between the two materials. This charge transfer with the Au surface results in a slight *p*-type doping of the graphene with a hole concentration of ~6.2x10^{11} holes/cm^2. The observed hole concentration is in good agreement with first principle predictions [69].

Substrate	k_f(Å^{-1})	ρ (cm^{-2})	doping type	E_{gap} (eV)
F-SiC [62]	-0.119	4.5x10^{13}	hole	
H-SiC [57]	-0.043	5.9 x10^{12}	hole	
Au-SiC [59]	-0.015	7.2 x10^{11}	hole	
Au(111)	**-0.014**	**6.2 x10^{11}**	**hole**	
Au-Ni(111) [70]	-0.014	6.2 x10^{11}	hole	
Au-Ru(0001) [72]	-0.014	6.2 x10^{11}	hole	
Ir(111) [37]	-0.013	5.4 x10^{11}	hole	
Cu-Ni(111) [70]	0.035	3.9 x10^{12}	electron	0.18
Ag-Ni(111) [70]	0.056	1.0 x10^{13}	electron	0.32
Cu(111) [60]	0.060	1.1 x10^{13}	electron	0.25
6√3 C-SiC [71]	0.075	1.8 x10^{13}	electron	0.00
Ru(0001) [72]	0.095	2.9 x10^{13}	electron	0.00

Table 5.1 Literature values for the Fermi vectors (k_f), doping level (ρ), doping type and gap size (E_{gap}) determined from ARPES measurements on various substrates. The graphene on Au(111) considered here is highlighted in bold. The doping level is determined using the size of the Fermi surface via the relation $\rho=k_f^2/(2\pi)$; gaps are provided for the *n*-doped samples only. Substrates labeled X - Y have X as an interface layer between the graphene and the substrate Y. Graphene on Au has almost as low a doping level as on Ir but maintains its characteristic band structure, making it an ideal candidate for studies of quasi-freestanding graphene.

Only graphene on Ir(111) displays a lower level of charge transfer. However, in that case the electronic structure of graphene is complicated by interactions with the Ir bands close to the Fermi level. The absence of these interactions in graphene on Au(111) makes this system well suited for investigations of quasi-free standing graphene. Recent studies of transferred and Au-intercalated graphene have taken advantage of this [70, 73-75].

The examination of graphene on Au(111) by ARPES offers no definitive explanation for the preference of the R0 orientation over the better lattice matched R30. Neither orientation experiences significant orbital hybridization with the substrate, as demonstrated by the preservation of the linear dispersion of free-standing graphene. Furthermore, both R0 and R30 orientations display the same charge transfer with the Au substrate, suggesting no material difference which might account for the preference. In addition to not differentiating between the R0 and R30 orientations, ARPES also shows a very weak overall interaction between the graphene and Au(111), regardless of orientation. This makes the orientational ordering even more puzzling. The interaction strength of graphene and a metal surface has been shown to be highly correlated with the degree or rotational ordering [15]. The single orientation of graphene on highly interacting Ru(0001) is the chief example of this [13]. Graphene growing on Ir, which is somewhat more weakly bound, has slightly more freedom and adopts multiple orientations [35]. We may draw further insight from the example of graphene on Ru(0001). Graphene and Ru(0001) have a similarly large lattice mismatch to graphene-Au(111), but well ordered epitaxy is nevertheless observed in that system. However, graphene on Au(111) has the curious combination of an extremely low interaction strength *and* a high degree of rotational ordering.

The absence of an energetic advantage for R0 over R30 graphene on Au(111) introduces the possibility that it is instead the result of growth kinetics. Such a kinetic preference could manifest itself during graphene nucleation on Au(111). For example, the R0 orientation of graphene could have a lower energetic barrier for nucleation or a smaller critical nucleus size. This would give it a higher possibility of initiating growth. Alternatively, the growth kinetics of the C crystal as it expands across the Au may also favor the R0 orientation. The geometric configuration of C atoms at the perimeter of the R0 graphene crystal might lower the energetic barrier to adatom attachment. However, this scenario is unlikely because the diffusion limited growth on Au(111) means that the vast majority of C atoms which impinge on a graphene island will become incorporated, regardless of the island edge configuration. Both these possibilities remain only speculation. Graphene grown on Au(111) achieves the degree of rotational homogeneity that has previously only been associated with graphene-metal systems which display a much stronger interaction between the two materials.

Regardless of its origin, the epitaxial fidelity between graphene and Au(111) leads to a substantially different domain size than growth on either Cu substrate.. The exceptional orientational homogeneity of the graphene islands makes this a fundamentally dissimilar situation. The precise in-plane alignment between neighboring islands means that they may combine with no crystallographic evidence of their separate nucleation events, such as a grain boundary. Domain size is not defined by the geometric extent of individual islands. This means large portions of the graphene film, comprising many formerly distinct islands, can be uninterrupted by rotational grain boundaries. Island coalescence of this type removes the significance of nucleation density and island size from determining the domain size. They are instead replaced by the degree of orientational homogeneity in the film. The final result of the coalescence of islands with the level of rotational alignment observed for graphene grown on Au(111) is a quasi-single crystal film which contains small regions of local rotational disorder. The regions of rotational disorder are the former graphene islands which possessed a non-R0 orientation prior to incorporation. The majority of these regions are rotated by 30º (the R30 islands). By fostering an even higher level of orientational ordering, the grain boundaries marking the perimeter these regions of rotational disorder may be limited. What methods may encourage further ordering is an open question. A sequence of experiments to optimize growth conditions such as deposition rate, surface quality, and growth temperature would provide a foundation for this effort. Together the distribution of relative orientations and domain size combine to make up the microstructure of graphene films grown on Cu(100), Cu(111), and Au(111).

Chapter 6 Graphene Film Nanostructure

6.1 Graphene and moiré patterns – Cu(111)

The nanoscale arrangement of graphene combines with its structure over the micron scale to determine the properties of the film. In the case of graphene on a (111) surface, be it Cu or Au, the common symmetry between the two materials leads to the formation of a two-dimensional moiré structure. Because these moiré patterns include a slight structural distortion of the graphene film, LEED is an effective method to observe their presence. Moiré patterns are a form of interference pattern; the unequal periodicity of the two overlaid lattices generates a lower frequency series of repeated geometric configurations of atoms. In the specific case of six-fold symmetric graphene on a six-fold symmetric metal surface, the moiré is also six-fold symmetric. This is shown by the diamond shaped unit cell of the moiré superlattice. For symmetry matched materials the periodicity of the moiré is governed by the difference in size between their surface unit cells and the relative angle between their lattices. Because the graphene lattice may rotate through a continuum on the metal surface, a corresponding range of moiré periodicities is possible. The size of the moiré unit cell may also be affected by deformation in either the graphene film or metal surface. For instance, moiré patterns coincide with out-of-plane corrugations in graphene films which cause a slight change to its effective periodicity within the plane. However, because these strains are usually very small this is only a secondary influence. Graphene on Ru(0001) again provides a helpful illustrative example. Because the film grows in only one relative orientation, it displays a single moiré pattern [45]. This moiré unit cell contains 25x25 graphene unit cells on top of 23x23 Ru surface cells, and is composed of two crystallographically inequivalent
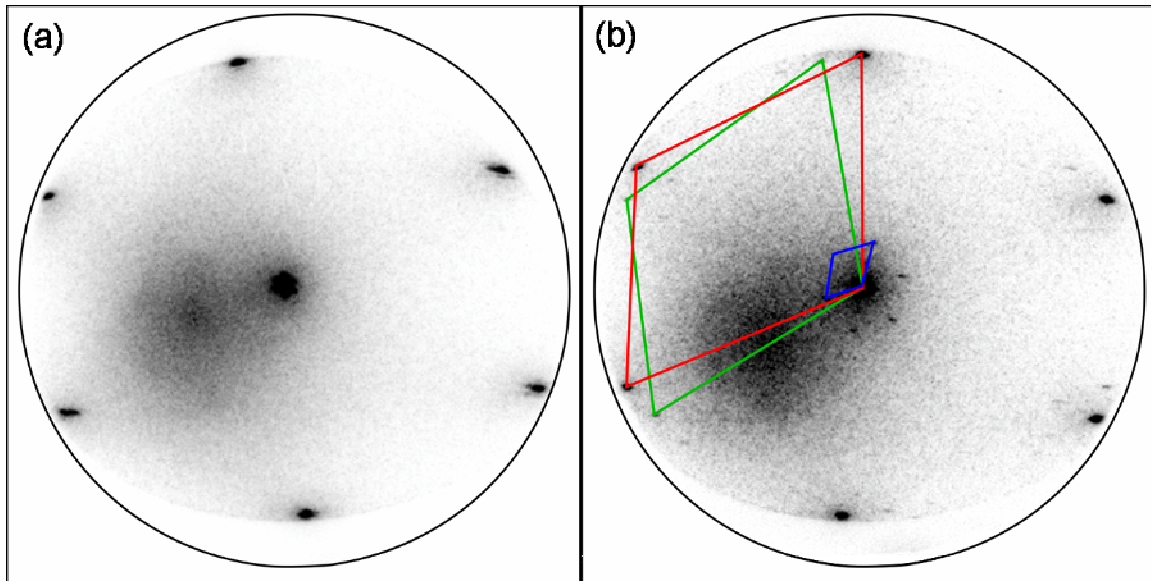
Figure 6.1   LEED patterns collected from graphene grown on Cu(111). The graphene crystal is very closely aligned with the Cu surface in **a**, leading to a very large moiré pattern, the diffraction spots of which are partially occluded by the specular beam. The graphene crystal (reciprocal unit cell shown in red) in **b** is rotated 6.5º from the Cu(111) surface (green), leading to a moiré with a much shorter periodicity (blue). Faint diffraction spots from the moiré are also visible around the first order graphene spots in **b**.

subcells. The graphene-Ru moiré structure also involves a 0.6-1.5 Å corrugation in the C film, and a distortion of the Ru crystal to a depth of multiple atomic layers [76]. In systems where the relative angle between the graphene and metal substrate adopts several discrete values, such as graphene on Ir(111), multiple moirés are observed [35]. Moiré superstructures analogous to those described for Ru and Ir were observed in graphene grown on Cu(111).

The nanoscale structure of graphene films on Cu(111) is a straightforward moiré. Neither the complex surface reconstruction of Au(111) nor the symmetry mismatch introduced by Cu(100) are present to complicate the scenario. The periodicity of the moiré pattern formed by graphene on Cu(111) tends to be large. Graphene has a relatively small ~3.8% lattice mismatch with Cu(111) and tends to align well with the substrate lattice. This leads to large lateral distances between repeated sets of specific atomic arrangements and thus low frequency moirés. We observe moiré periodicities ranging from 7.5 Å for graphene rotated by 27.5º to >60 Å from graphene aligned with the Cu(111) surface. However, the diffraction spots generated by the largest moirés are partially obscured by the specular beam, as is the case in **Figure 6.1.a**. This makes precise measurement of their periodicity difficult. The space between these extremes is occupied by a continuum of other moiré periodicities, an example LEED pattern of which is shown in **Figure 6.1.b**. The periodicities of the graphene moiré on Cu(111) measured here by LEED agree well with recent measurements using STM [44]. The moiré pattern formed by graphene on a metal becomes increasingly more complicated as the surface on which it rests deviates from the ideal close-packed configuration.

6.2 The 1-dimensional superstructure of graphene on Cu(100)

Graphene grown on Cu(100) is an example of how a different substrate symmetry affects the superstructure adopted by the system. As was discussed in Chapter 3 the combined symmetry of the graphene-Cu(100) system results in a two-fold symmetric growth velocity. In a similar manner, the six-fold symmetry of graphene overlaid on the four-fold symmetric Cu surface generates a symmetry axis in the resulting nanoscale structure. The only shared in-plane symmetry element of the p6m graphene and p4m Cu surface is a 180º rotation. It is this shared element which dictates the symmetry of the superstructure. Selected-area LEED from a single graphene domain on Cu(100) largely exhibits the features thatone would expect. The hexagonal first-order pattern from the graphene surrounds the slightly smaller, four-fold pattern of the Cu surface. Examples of this are included in **Figure 6.2.a** and **.b**. There are commonly two additional points of high intensity in the LEED pattern symmetrically situated close to the specular beam. These spots can be seen in **Figure 6.2.a**, but are absent in **Figure 6.2.b**. Additional spots are generally observed when the graphene domain in question is within ~±10º of being aligned with the Cu surface. The distance between the extra spots and the specular beam is variable. By comparing the radii of the extra spots with those of the graphene and Cu lattices, it is possible to determine that they result from physical phenomena with a periodicity ranging from 10.5 Å to 14.9 Å. Recent STM studies of graphene on Cu(100)
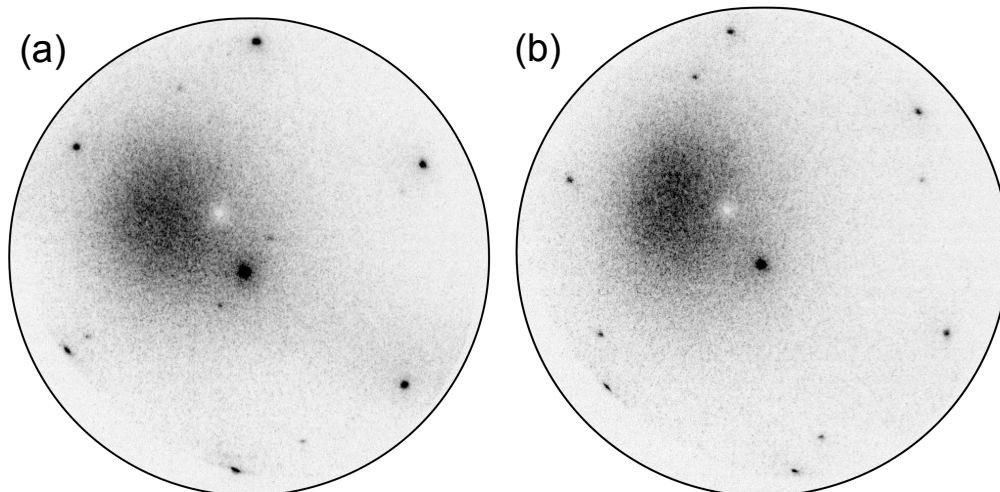
Figure 6.2 LEED collected from graphene grown on Cu(100). When the graphene lattice is within ±10° of aligned with the Cu surface, as is the case in **a** where it is rotated by 4°, two extra diffraction spots near the specular beam are apparent. These two additional spots are attributable to the linear, 1-dimensional ridged moiré of graphene on the symmetry mismatched (100) Cu surface. When the lattice is rotated by more than 10°, as is shown in **b** where it is rotated by 13.5°, the moiré spots are not apparent.

have revealed a superstructure composed of ridges in the graphene film. Ridge wavelengths of 11 Å [77], 12±1 Å [78], and 13.5 Å [79] were reported. The symmetry and periodicity of this superstructure matches what would be expected from the extra spots observed by LEED. Thus we conclude that the additional LEED spots are attributable to a surface structure composed of linear corrugations in the graphene film. This also makes clear that LEED is an appropriate method with which to characterize the structure. In addition to varying in radius from the specular beam, the diffraction spots from the one-dimensional surface superstructure also rotate relative to the Cu and graphene patterns. The observed rotations indicate the one-dimensional moiré may have any orientation on the surface.

Because the two-fold superstructure of graphene on Cu(100) is dictated by the symmetries of the two materials, its specific details must also depend on their relative orientation. This is again akin to the growth rate of graphene on Cu(100). Selected-area LEED patterns displaying a range of different graphene orientations were analyzed to ascertain this dependence. The LEED patterns inspected included the full range of the most common graphene orientations, covering a ~18° arc centered on a Cu[011] direction as **Figure 5.1.a** shows. This analysis is summarized in **Figure 6.3**. It reveals that both the orientation and wavelength of the superstructure depend on the graphene-to-Cu orientation. As the graphene lattice swivels from +9° to -9° the orientation of the one-dimensional moiré rotates by ~90°. It starts parallel to Cu<010>, moves through Cu<01$\bar{1}$> when the graphene lattice is aligned with the Cu surface, and ends parallel to Cu<00$\bar{1}$>. The periodicity of the ridges varies simultaneously. The shortest wavelength of 10.5 Å corresponds to the superstructure parallel to a Cu[010] direction, and the longest of 14.9 Å occurs when it is parallel to a Cu[01$\bar{1}$] direction. When the graphene lattice is aligned with the Cu surface (C(01) parallel to Cu(011)), the ridges are parallel to a zigzag direction, and perpendicular to an armchair direction. At this point the superstructure is
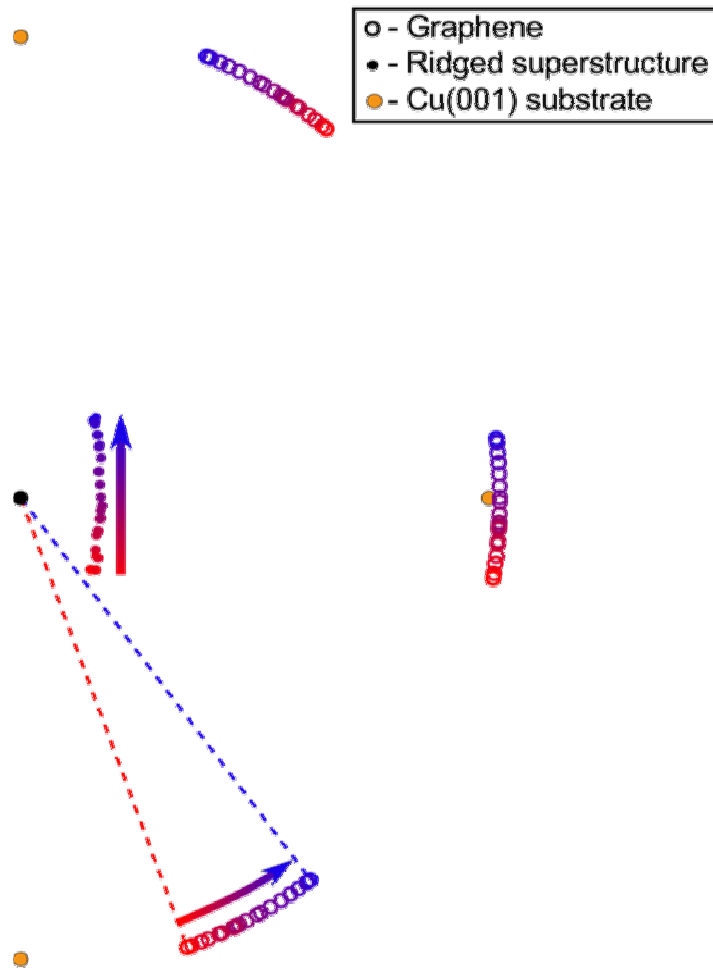
Figure 6.3 LEED diagram of graphene on Cu(100), made from a composite of individual patterns, showing the dependence of the linear moiré orientation and periodicity on the graphene rotation. Each color spot, ranging from red to blue, corresponds with the location of diffractions spots from a particular LEED pattern. As the graphene sheets rotate from -9º to +9º, the moiré orientation rotates by 90º from Cu<0$\bar{1}$0> to Cu<001>.

also at its longest wavelength. The one-dimensional moiré of graphene on Cu(100) is a consequence of the symmetry mismatch between the materials. Its orientation and periodicity depend on the relative orientation of the graphene lattice and Cu(100) surface. Furthermore, a closer examination of this dependence reveals that the graphene-Cu interaction imposes additional constraints on the configuration of the superstructure.

One immediately noticeable feature of the ridged structure of graphene on Cu(100) is that its wavelength projected along the Cu(01$\bar{1}$) direction remains constant. This is true as both its orientation and overall periodicity shift in response to changes in the angle between the two materials. The sequence of moiré diffractions spots which form a line perpendicular to Cu(01$\bar{1}$) in **Figure 6.3** shows this. It is perhaps helpful to visualize cutting the graphene film along the Cu(01$\bar{1}$) direction: no matter what the orientation and wavelength of the superstructure, the exposed cut edge of the graphene

film has the same shape. The steady wavelength along Cu(01$\bar{1}$) of ~14.9 Å corresponds to ~5.8 Cu(100) surface unit cells. This periodicity along Cu(01$\bar{1}$) is preserved as the one-dimensional moiré rotates through a full 90º arc. With symmetry, this range of orientations comprises any possible configuration of the superstructure on the surface.

Graphene domains within ±10º of alignment with the lattice of a Cu(100) substrate form a well defined ridged moiré. But what structure exists in the rarer regions of graphene which are rotated by ±10-15º? As graphene approaches a ±15º misalignment on a (100) surface, it begins to develop a particular symmetry condition: the effective graphene structure along all four Cu[01$\bar{1}$] in-plane directions becomes degenerate. The bonding along these particular crystallographic directions dictates the details of the superstructure as is demonstrated by its constant periodicity along them. Because of this the symmetry condition which required a two-fold structure is broken. The surface structure resulting from these alignments is similar to two interwoven one-dimensional moirés. Graphene-Cu(100) superstructures resembling precisely this have indeed been observed by STM [78, 79]. A particularly fine example is that included by Rassol *et al.* [79]. The surface of the graphene domain, which is rotated by 17º on Cu(100) (which is equivalent to 13º, by symmetry), shows almost perfect square symmetry [79]. The absence of an observable LEED pattern from this second surface structure is probably due to a combination of two different effects. The lack of a clearly defined preferred configuration likely leads to increased local disorder in the superstructure. Such slight variations in periodicity and orientation would reduce the constructive interference necessary for a diffraction peak. The increased disorder in the surface structure may also reduce the amplitude of the corrugations in the graphene layer, further attenuating diffraction. The combination of enhanced local disorder and decreased corrugation amplitude could be sufficient to quench any detectable LEED pattern. The observation that the intensity of the LEED spots associated with the one-dimensional moiré decreases as the graphene lattice rotates away from alignment with the Cu surface supports this supposition. Regardless of the relative orientation of the two materials, it is the interaction between graphene and Cu(100) along the [01$\bar{1}$] in-plane Cu directions that determines the formation of the surface structure.

Although the details of the one-dimensional moiré formed by graphene on Cu(100) are clear, any potential significance of it's constituent ridges during growth is not. The coincidence of the most highly ordered moiré structure with the most commonly occurring graphene orientations suggests a correlation between the two. This relationship could be a result of energy minimization if the moiré pattern of aligned graphene is the lowest energy configuration of the interface. The "effort" put into maintaining the periodicity of the graphene ridges along the Cu close-packed directions lends credence to this possibility. A link between the moiré structure of graphene on Cu(100) and its growth behavior might also be based on the kinetic process of C atoms joining the graphene crystal during growth. The intersection of the ridges in the graphene with the perimeter of the crystal likely changes the structure of the edge. The changes induced by the moiré would be significant because the attachment limited growth of graphene on Cu(100) depends on the specific configuration of atoms at the growth front. However, the lack of a discernable difference in growth rate for graphene domains over a

range of orientations casts doubt on this possibility. Finally, it is also possible that the one-dimensional moiré is an artifact of the nucleation process of graphene on Cu(100). If a pre-graphene C configuration bonded with the Cu surface in this way it could be preserved throughout the subsequent expansion of the domain. Yet the propensity of graphene for heterogeneous nucleation, and the subsequent orientation selection process which unfolds on Cu(100), make this an unlikely explanation. Despite the likelihood of a causal relationship between the preferred relative orientations of graphene on Cu(100) and the corresponding one-dimensional moirés, its specifics remain unknown. The symmetry mismatch between graphene and Cu(100) results in a one-dimensional moiré of ridges in the C film.

6.3 The graphene moiré and the Au(111) herringbone surface reconstruction

Although the moiré patterns of graphene on Cu(111) and Au(111) are fundamentally the same, the additional complexity of the Au surface produces a more involved structure. The outermost layer of atoms of a Au crystal has a slightly higher density than the bulk of the material. On the (111) facet this layer adopts a "herringbone" surface reconstruction made up of a periodic array of surface dislocations [59]. The increased density of the surface of Au is a result of the atoms attempting to compensate for their reduced coordination by shortening their bond length with their nearest neighbors. Surface dislocations become necessary to maintain coherency between the denser surface layer and the bulk. In the case of Au(111), these dislocations become ordered into a chevron-like distribution with a periodicity of 6 nm, leading to the "herringbone" structure. This ordering of the surface dislocations is broken when the crystal is heated above 592 ºC. The resulting disordered surface phase nonetheless maintains a higher density than bulk Au [80]. The dislocation ordering which leads to the herringbone appearance of the Au(111) surface persists in the presence of a graphene overlayer, and influences the resulting graphene moiré.

Scanning tunneling microscopy is a more constructive characterization technique in the case of the superstructure of graphene on Au(111). As shown in **Figure 6.4**, the herringbone surface reconstruction generates a corresponding diffraction pattern. These additional diffraction spots are difficult to unambiguously discern from the moiré LEED pattern and may directly obscure it. An example of a STM image taken from an R0-oriented graphene domain grown on Au(111) is shown in **Figure 6.5.a**. Both the graphene moiré and Au herringbone structures are immediately apparent in the image. The moiré pattern can be seen in the very slight depressions in the graphene. As expected for the six-fold symmetric graphene on a (111), close packed surface the depressions are arranged in a hexagonal array. The depressions are 0.15 Å deep and spaced with a <2 nm periodicity. Superimposed are the faint ribbons of the herringbone. These bend from nearly horizontal in the upper-left part of the image to nearly vertical in the lower right part. In this case, the ribbons of the herringbone reconstruction have the same dimensions as those on a bare Au(111) facet. The influence of the persistent Au(111) surface reconstruction can be seen where the moiré crosses a herringbone domain boundary. Both the moiré periodicity and orientation are slightly distorted.
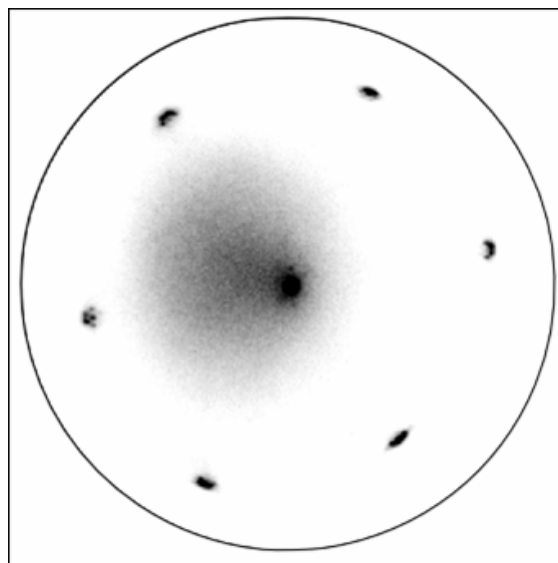
Figure 6.4 LEED pattern of a clean, bare Au(111) surface. Au(111) develops a herringbone surface reconstruction, diffraction from which can be seen in the superstructure surrounding each Au diffraction spot.

The main features of STM images of graphene grown on Au(111) can all be accounted for without having to invoke any lateral distortions in the graphene lattice. The following simple atomic model demonstrates this fact and is illustrated in **Figure 6.5.b**. For this model we generated the Au(111) surface employing a 2-dimensional Frenkel-Kontorova algorithm [81]. A unit cell of the Au herringbone reconstruction is shown in the upper part of **Figure 6.5.b**. A graphene lattice is placed onto the Au surface
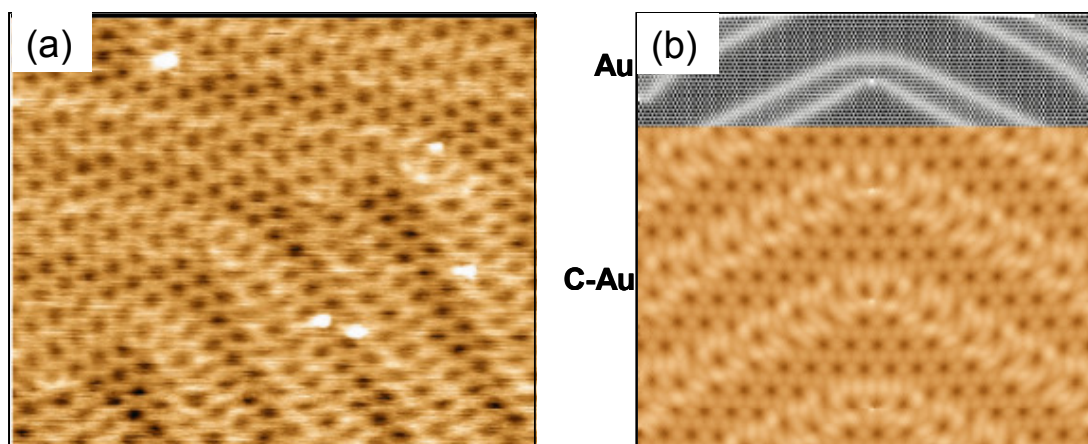
Figure 6.5 Scanning tunneling microscopy of graphene on Au(111). (**a**) 35 nm x 29 nm STM image of R0 graphene. The hexagonal array of depressions, 0.15 deep and <2 nm far apart, is due to the moiré between the uppermost Au atoms and the graphene layer. Superimposed are faint ribbons 6 nm apart, which bend from nearly horizontal in the upper-left part of the image to nearly vertical in the lower right part. The ribbons have the same dimensions as the "herringbone" dislocation pattern of the reconstructed Au(111) surface. (**b**) Image simulations of the STM image **a** based on a simple atomic model. The Au(111) surface [an exposed region is shown at the top of **b**] is covered by a laterally undistorted R0-oriented graphene lattice. The brightness of the model surface is determined by the distortions of the Au lattice as well as the lateral positions of the C atoms with respect to the Au substrate (e.g., on-top positions are bright). That graphene-covered Au develops the same dislocation structure as the bare Au(111) surface highlights how little the gold is affected by the presence of graphene. The author would like to acknowledge Dr. Norm Bartelt and Dr. Konrad Thürmer of Sandia National Laboratories.

without allowing the graphene sheet to relax laterally. To simulate the STM image the brightness is estimated as a function of the lateral positions of the C atoms with respect to the underlying Au lattice (e.g., on-top positions are bright and three-fold hollow sites are dark as described in [35]) as well as the amount of local distortion in the Au lattice.

The fact that the Au(111) herringbone surface reconstruction persists even when it is covered by an epitaxial graphene film gives further insight into the interaction between the two materials in this system. The ordering of a bare Au surface into the herringbone structure is the result of a delicate energy balance that, remarkably, is not tipped by the presence of the graphene [59]. Further analysis of the STM images presented here has allowed for the establishment of an upper bound for the bond strength between graphene and Au. Because the herringbone pattern is undisturbed and has the same periodicity as observed on a bare Au(111) surface, the bond strength between the graphene and Au may be no more than 13 meV per C atom [82]. This is consistent with the ARPES discussed in Chapter 5 and further emphasizes the exceptional degree to which the graphene and Au surface are decoupled. The minimal influence exerted on the graphene film by the Au substrate, and vise-versa, is also shown by the absence of lateral atomic distortions in the STM images. Furthermore, the Au atoms at the graphene interface are sufficiently mobile to allow the Au surface dislocations to reorganize during sample cooling from their disordered state at the growth temperature. The moiré pattern of graphene on Au(111) is an interesting example of how metal surface reconstructions influence hetero-superstructures. It also offers further evidence of the degree to which graphene and Au(111) are decoupled.

Chapter 7 Conclusion

7.1 Summary of Findings

The substrates investigated here illicit a range growth behaviors from graphene, which in turn generate variations in the structure of the resulting films. The combination of low-energy electron microscopy and diffraction is a powerful suite of tools for identifying the fundamental processes that underpin these behaviors. The appropriate application of complementary characterization techniques makes LEEM and LEED even more potent. As this dissertation has shown with these tools, the growth behavior of graphene varies substantially even between superficially similar substrate surfaces.

Even at the elevated temperatures used for graphene growth both Cu and Au have negligible C solubility. Their resulting ability to support monolayer graphene growth removes the potential complexity of multiple C layers. This allows other experimental variables to be more easily isolated. Two such variables of focus here were substrate symmetry and metal-substrate species. The impact of varying the substrate symmetry was examined by synthesizing graphene on both the (100) and (111) facets of Cu. By exploring graphene growth on the (111) faces of both Cu and Au, it was possible to observe the influence of the substrate material.

Graphene nucleates heterogeneously on the (100) facet of Cu. Each nucleation site seeds multiple graphene crystals, as differentiated by their respective rotations about the film normal. The multiple graphene crystals grow contiguously to comprise an individual island. A selection process occurs soon after nucleation which results in four preferentially oriented graphene domains coming to dominate each island. These four crystals cause the island to develop a distinct four-lobed morphology. The long axes of the graphene lobes tend to align from island to island, leading to a patterned substrate surface. The simultaneous evaporation of Cu during growth causes substantial step flow on the substrate surface. Mobile Cu steps decelerate as they travel beneath a graphene island. This deceleration causes step bunching and eventually substantial accumulation. As a result of this process "hillocks" of Cu form which reflect the morphology of the overlying C. The polycrystalline nature of graphene islands on Cu(100) adds complexity to their process of shape evolution. The behavior of individual C domains must be distilled from this.

The governing determinant in the shape evolution of individual graphene crystals on Cu(100) is their attachment limited growth mode. The attachment limited growth mode and the symmetry mismatch between the two materials leads graphene to have a two-fold symmetric, angularly dependent growth rate. This is the origin of the distinct elongation of the graphene island lobes. Graphene's angularly dependent growth rate is also influenced by the relative orientation between the two materials. The distribution of relative orientations between graphene and Cu(100) is centered on two crystallographically degenerate configurations with a substantial spread of ±10º around each of these. The multi-domain structure of individual islands and the overall nucleation density lead to average graphene domain sizes of 10-20 μm. Because of the significant

rotational variation between them, the graphene domains developed during growth remain physically distinct upon incorporation into a complete film. The symmetry mismatch which governs graphene's growth behavior is also evident in the nanoscale structure of the film. Graphene on Cu(100) develops a superstructure composed of ridges in the graphene film. The orientation and wavelength of these ripples are dependent on the angle between the graphene lattice and Cu surface. Perhaps surprisingly, many of the characteristic behaviors of graphene growth on Cu(100) are not evident during synthesis on the (111) facet.

Similar to growth on Cu(100), initial graphene nucleation on Cu(111) usually happens heterogeneously. Graphene islands that nucleate later tend to do so homogeneously. The sites where this secondary homogeneous nucleation occurs show a strong correlation with regions of high C adatom concentration. This is one of many ways in which surface diffusion of C adatoms and adatom species influences graphene growth on Cu(111). Interestingly, the distribution of crystalline domains within the graphene islands is largely determined by the type of nucleation the island undergoes. Islands that nucleate heterogeneously are typically composed of multiple crystallographic domains, akin to the internal structure of graphene islands on Cu(100). Homogeneous nucleation generally yields islands composed of only a single constituent domain. This is indicative of a system where the energetic landscape is relatively flat with respect to the relative orientation between the two materials; an observation born out by the ±3° spread of rotations adopted by graphene around the ideal, aligned orientation. The existence of a single high-symmetry configuration of graphene on the (111) surface is an important difference from the degeneracy on the (100) facet.

The significance of surface diffusion is also apparent in the dendritic shapes of graphene islands grown on Cu(111). This is particularly pronounced in growths performed at lower temperatures. The degree of ramification varies dramatically across the temperature range which can be used for growth with islands at higher temperatures maintaining a faceted morphology to much larger sizes. This points out the temperature dependence of the C ad-species diffusivity. It also shows the curious coincidence that the diffusion length and the size of the islands are of the same magnitude, even inverting as the C islands expand. It is possible to directly observe the influence of diffusion on growth by comparing the observed growth rate of a set of graphene islands with a numerical solution to the diffusion equation for that particular surface geometry. Predictions of the ad-species flux experienced by the graphene growth front match the recorded growth rate very closely. When growth on Cu(111) is allowed to proceed to completion the resulting polycrystalline graphene film is comprised of domains similar in size to those on Cu(100). The ~10 μm grains have a smaller spread of out-of-plane rotations, only ±3°. Unlike on the (100) facet substrate step edges on Cu(111) are not innocuous. Propagating graphene growth fronts which intersect a large Cu step bunch often adopt a different orientation as they grow across the bunch. This results in increased crystalline disorder in the C film. Because the graphene and Cu surface are symmetry matched the graphene film develops a hexagonal moiré superstructure. The periodicity and orientation of this superstructure also depends on the relative orientation of that particular domain. The periodicity ranges from ~60 Å when the two materials are

closely aligned, to ~7.5 Å in the significantly rotated domains. The final micro- and nanostructure of graphene films grown on Cu(111) reflect a decrease in crystalline disorder from those synthesized on the (100) facet. This trend is further extended when these substrates are compared to Au(111).

Au(111) presents an interesting comparative substrate study when combined with the Cu facets. It has a substantially larger unit cell than Cu and thus potentially a correspondingly higher lattice mismatch. It also forms the distinct herringbone surface reconstruction on its (111) facet. Graphene islands nucleate, both homogeneously and heterogeneously, in a much higher density on Au than they do on Cu. These islands have already developed a dendritic structure when they become resolvable in LEEM. The very early onset of dendritic growth suggests an extremely short diffusion distance for the C species involved. While graphene islands that grow unperturbed form six-fold symmetric crystals, those on a Au step propagate much more quickly parallel along the step. This results in an elongated island profile. Despite its significantly higher lattice mismatch, over 95% of graphene islands adopt the "R0" orientation on graphene. The precise inter-island alignment of these crystals allows them to merge without necessarily requiring a grain boundary to accommodate the intersection of their respective lattices. Instead of individual island size and constituent crystalline composition governing the domain size, rather the degree of epitaxial fidelity between C and Au is the determining factor. Thus, these films are quasi-single crystal with rotational defect confined to small localized regions.

That graphene adopts the R0 orientation rather than one with a 30º rotation, and the extent to which it does so, is surprising given the minimal interaction between the two materials. ARPES offers no evidence for the origin of the R0 preference. Both R0 and R30 orientations maintain the linear dispersion of free standing graphene. Furthermore, the extent of charge transfer with the substrate is the same regardless of orientation. STM reveals that the Au(111) herringbone surface reconstruction persists even while covered by an epitaxial graphene film. This offers further evidence of the extremely weak interaction between the two materials. A significant bond would interrupt the delicate energy balance which causes the chevron like herringbone. A careful analysis of the graphene-herringbone structure allows an upper bound of 13 meV per C atom to be set for the graphene-Au bond. The combination of extraordinary eptiaxial fidelity and a high density of small islands makes growth on Au(111) a fundamentally new pathway to reducing the crystalline disorder in graphene films.

7.2 Future directions

As graphene moves from bench-top curiosity to part of our technological infrastructure, controllable and scalable synthesis methods will become increasingly important. Understanding its growth behavior on Cu(100), Cu(111), and Au(111) offers important insights towards this goal. Despite similarities, such as low interaction strengths relative to other metals, graphene growth on these surfaces displays a range of behaviors. The differences in nucleation and growth mechanisms yield corresponding

variations in the micro- and nanostructure of the resulting films. The fundamental properties which underlie these behaviors are crucial to facilitate the optimization of graphene growth for both scientific and technological purposes.

The past few years have seen remarkable progress in understanding these fundamentals. Despite this, there remain many open questions about graphene growth on low-C solubility substrates. Identifying why the graphene-Cu(100) interaction leads to an attachment limited growth mode is one of these questions. There are a number of different approaches to address this issue. Continuing to explore graphene growth on different substrates may well offer important clues. In particular, observing graphene growth on Cu(110) would provide further insight into the nature of the graphene-Cu interaction. It would also be interesting to see if shifting from the (111) to the (100) facet of Au produces a similar change in growth mode. Because graphene growth on low-C solubility metals is likely to become increasingly important it is imperative to understand the fundamental processes which underpin this synthesis method.

In addition to continued development of growth on low-C solubility substrates there are broader issues facing the field graphene synthesis. The first of these is the uncertainty regarding the quality of graphene required for applications. Exactly what level of crystalline quality a graphene film needs to have for most potential applications remains an open question. For instance, experimentally quantifying the impact of grain boundaries on electrical transport in graphene is a prerequisite for efficient progress in its synthesis. The process of transferring graphene off metal substrates is another cumbersome aspect of current graphene growth methods. If this transfer process proves unavoidable, research such as the roll-to-roll graphene fabrication performed at Samsung [30] will need to be vigorously pursued. It would be ideal to avoid transferring by instead depositing directly on dielectric substrates. However, growth on dielectrics has yet to yield graphene of sufficient quality [83-85]. As discussed in Appendix B, Ge shows promise as a possible alternative. A more specific and nuanced vision of where the field of graphene synthesis needs to reach is an important factor in facilitating the continued development of the material. Improved synthesis methods are vital if graphene is to fulfill its potential and a scientific and technological material.

References

1. Wallace, P.R., *The Band Theory of Graphite.* Physical Review, 1947. **71**(9): p. 622-634.
2. Slonczewski, J.C. and P.R. Weiss, *Band Structure of Graphite.* Physical Review, 1958. **109**(2): p. 272-279.
3. Novoselov, K.S., et al., *Electric field effect in atomically thin carbon films.* Science, 2004. **306**(5696): p. 666-669.
4. Novoselov, K.S., et al., *Two-dimensional gas of massless Dirac fermions in graphene.* Nature, 2005. **438**(7065): p. 197-200.
5. Zhang, Y.B., et al., *Experimental observation of the quantum Hall effect and Berry's phase in graphene.* Nature, 2005. **438**(7065): p. 201-204.
6. Novoselov, K.S., et al., *Room-temperature quantum hall effect in graphene.* Science, 2007. **315**(5817): p. 1379-1379.
7. Geim, A.K. and K.S. Novoselov, *The rise of graphene.* Nature Materials, 2007. **6**(3): p. 183-191.
8. Yu, Q.K., et al., *Graphene segregated on Ni surfaces and transferred to insulators.* Applied Physics Letters, 2008. **93**(11): p. 113103.
9. Sun, C.Q., et al., *Dimension, strength, and chemical and thermal stability of a single C-C bond in carbon nanotubes.* Journal of Physical Chemistry B, 2003. **107**(31): p. 7544-7546.
10. Ryu, S., et al., *Atmospheric Oxygen Binding and Hole Doping in Deformed Graphene on a SiO(2) Substrate.* Nano Letters, 2010. **10**(12): p. 4944-4951.
11. Bolotin, K.I., et al., *Ultrahigh electron mobility in suspended graphene.* Solid State Communications, 2008. **146**(9-10): p. 351-355.
12. Castro Neto, A.H., et al., *The electronic properties of graphene.* Reviews of Modern Physics, 2009. **81**(1): p. 109-162.
13. Sutter, P.W., J.I. Flege, and E.A. Sutter, *Epitaxial graphene on ruthenium.* Nature Materials, 2008. **7**(5): p. 406-411.
14. Zhou, S.Y., et al., *Substrate-induced bandgap opening in epitaxial graphene.* Nature Materials, 2007. **6**(10): p. 770-775.
15. Preobrajenski, A.B., et al., *Controlling graphene corrugation on lattice-mismatched substrates.* Physical Review B, 2008. **78**(7): p. 073401.
16. Ohta, T., et al., *Controlling the electronic structure of bilayer graphene.* Science, 2006. **313**(5789): p. 951-954.
17. Zhang, Y., et al., *Direct observation of a widely tunable bandgap in bilayer graphene.* Nature, 2009. **459**(7248): p. 820-823.
18. Taychatanapat, T., et al., *Quantum Hall effect and Landau-level crossing of Dirac fermions in trilayer graphene.* Nature Physics, 2011. **7**(8): p. 621-625.
19. Sanchez-Yamagishi, J.D., et al., *Quantum Hall Effect, Screening, and Layer-Polarized Insulating States in Twisted Bilayer Graphene.* Physical Review Letters, 2012. **108**(7): p. 076601.
20. Partoens, B. and F.M. Peeters, *From graphene to graphite: Electronic structure around the K point.* Physical Review B, 2006. **74**(7): p. 075404.
21. Wang, X.R., et al., *N-Doping of Graphene Through Electrothermal Reactions with Ammonia.* Science, 2009. **324**(5928): p. 768-771.

22. Wehling, T.O., et al., *Molecular doping of graphene.* Nano Letters, 2008. **8**(1): p. 173-177.

23. Wei, D.C., et al., *Synthesis of N-Doped Graphene by Chemical Vapor Deposition and Its Electrical Properties.* Nano Letters, 2009. **9**(5): p. 1752-1758.

24. Han, M.Y., et al., *Energy Band-Gap Engineering of Graphene Nanoribbons.* Physical Review Letters, 2007. **98**(20): p. 206805.

25. Lin, Y.M., et al., *100-GHz Transistors from Wafer-Scale Epitaxial Graphene.* Science, 2010. **327**(5966): p. 662-662.

26. Robinson, J.T., et al., *Wafer-scale Reduced Graphene Oxide Films for Nanomechanical Devices.* Nano Letters, 2008. **8**(10): p. 3441-3445.

27. Zhou, M., Y.M. Zhai, and S.J. Dong, *Electrochemical Sensing and Biosensing Platform Based on Chemically Reduced Graphene Oxide.* Analytical Chemistry, 2009. **81**(14): p. 5603-5613.

28. Robinson, J.T., et al., *Reduced Graphene Oxide Molecular Sensors.* Nano Letters, 2008. **8**(10): p. 3137-3140.

29. Schedin, F., et al., *Detection of individual gas molecules adsorbed on graphene.* Nature Materials, 2007. **6**(9): p. 652-655.

30. Bae, S., et al., *Roll-to-roll production of 30-inch graphene films for transparent electrodes.* Nature Nanotechnology, 2010. **5**(8): p. 574-578.

31. Charrier, A., et al., *Solid-state decomposition of silicon carbide for growing ultra-thin heteroepitaxial graphite films.* Journal of Applied Physics, 2002. **92**(5): p. 2479-2484.

32. Stankovich, S., et al., *Synthesis of graphene-based nanosheets via chemical reduction of exfoliated graphite oxide.* Carbon, 2007. **45**(7): p. 1558-1565.

33. Loginova, E., et al., *Evidence for graphene growth by C cluster attachment.* New Journal of Physics, 2008. **10**: p. 093026.

34. Loginova, E., et al., *Factors influencing graphene growth on metal surfaces.* New Journal of Physics, 2009. **11**: p. 063046.

35. Loginova, E., et al., *Defects of graphene on Ir(111): Rotational domains and ridges.* Physical Review B, 2009. **80**(8): p. 085430.

36. McCarty, K.F., et al., *Kinetics and thermodynamics of carbon segregation and graphene growth on Ru(0001).* Carbon, 2009. **47**(7): p. 1806-1813.

37. Starodub, E., et al., *In-plane orientation effects on the electronic structure, stability, and Raman scattering of monolayer graphene on Ir(111).* Physical Review B, 2011. **83**(12): p. 125428.

38. Li, X.S., et al., *Transfer of Large-Area Graphene Films for High-Performance Transparent Conductive Electrodes.* Nano Letters, 2009. **9**(12): p. 4359-4363.

39. Li, X.S., et al., *Large-Area Synthesis of High-Quality and Uniform Graphene Films on Copper Foils.* Science, 2009. **324**(5932): p. 1312-1314.

40. Li, X.S., et al., *Graphene Films with Large Domain Size by a Two-Step Chemical Vapor Deposition Process.* Nano Letters, 2010. **10**(11): p. 4328-4334.

41. Li, X.S., et al., *Evolution of Graphene Growth on Ni and Cu by Carbon Isotope Labeling.* Nano Letters, 2009. **9**(12): p. 4268-4272.

42. Wofford, J.M., et al., *Graphene Islands on Cu Foils: The Interplay between Shape, Orientation, and Defects.* Nano Letters, 2010. **10**(12): p. 4890-4896.

43.   Sutter, P., J.T. Sadowski, and E. Sutter, *Graphene on Pt(111): Growth and substrate interaction.* Physical Review B, 2009. **80**(24): p. 245411.

44.   Gao, L., J.R. Guest, and N.P. Guisinger, *Epitaxial Graphene on Cu(111).* Nano Letters, 2010. **10**(9): p. 3512-3516.

45.   Martoccia, D., et al., *Graphene on Ru(0001): A 25x25 supercell.* Physical Review Letters, 2008. **101**(12): p. 126102.

46.   Murata, Y., et al., *Moire Superstructures of Graphene on Faceted Nickel Islands.* Acs Nano, 2010. **4**(11): p. 6509-6514.

47.   Nie, S., et al., *Growth from Below: Graphene Bilayers on Ir(111).* Acs Nano, 2011. **5**(3): p. 2298-2306.

48.   Strauman.Me and L.S. Yu, *Lattice Parameters, Densities, Expansion Coefficients and Perfection of Structure of Cu and of Cu-In Alpha Phase.* Acta Crystallographica Section a-Crystal Physics Diffraction Theoretical and General Crystallography, 1969. **A 25**: p. 676-.

49.   Maeland, A. and T.B. Flanagan, *X-ray and Thermodynamic Studies of Absorption of Hydrogen by Gold-Palladium Alloys.* Journal of Physical Chemistry, 1965. **69**(10): p. 3575-.

50.   Barrett, C.S.M., T. B., *Structure of Metals.* 1980, Elmsford, NY: McGraw-Hill.

51.   Bauer, E., *Low-Energy-Electron Microscopy.* Reports on Progress in Physics, 1994. **57**(9): p. 895-938.

52.   Ferrari, A.C., et al., *Raman spectrum of graphene and graphene layers.* Physical Review Letters, 2006. **97**(18): p. 187401.

53.   Herring, C., *Some Theorems On the Free Energies of Crystal Surfaces.* Physical Review, 1951. **82**(1): p. 87-93.

54.   Frank, F.C. in *Proceedings of an International Conference on Crystal Growth.* 1958. Cooperstown, NY: Wiley, NY.

55.   Fu, T.Y., H.T. Wu, and T.T. Tsong, *Energetics of surface atomic processes near a lattice step.* Physical Review B, 1998. **58**(4): p. 2340-2346.

56.   Meyer, J.A., et al., *Importance of the additional step-edge barrier in determining film morphology during epitaxial-growth.* Physical Review B, 1995. **51**(20): p. 14790-14793.

57.   Kyuno, K. and G. Ehrlich, *Step-edge barriers: truths and kinetic consequences (vol 383, pg 766, 1986).* Surface Science, 1997. **394**(1-3): p. L179-L187.

58.   Nie, S., et al., *Origin of the mosaicity in graphene grown on Cu(111).* Physical Review B, 2011. **84**(15): p. 155425.

59.   Narasimhan, S. and D. Vanderbilt, *Elastic Stress Domains and the Herringbone Reconstruction on Au(111).* Physical Review Letters, 1992. **69**(10): p. 1564-1567.

60.   Nix, F.C. and D. MacNair, *The thermal expansion of pure metals copper, gold, aluminum, nickel, and iron.* Physical Review, 1941. **60**(8): p. 597-605.

61.   Yazyev, O.V. and S.G. Louie, *Electronic transport in polycrystalline graphene.* Nature Materials, 2010. **9**(10): p. 806-809.

62.   Yazyev, O.V. and S.G. Louie, *Topological defects in graphene: Dislocations and grain boundaries.* Physical Review B, 2010. **81**(19): p. 195420.

63.   Colombo, L., et al., *Growth Kinetics and Defects of CVD Graphene on Cu.* ECS Transactions, 2010. **28**(5): p. 109-114.

64. Li, X.S., et al., *Large-Area Graphene Single Crystals Grown by Low-Pressure Chemical Vapor Deposition of Methane on Copper.* Journal of the American Chemical Society, 2011. **133**(9): p. 2816-2819.

65. Yu, Q.K., et al., *Control and characterization of individual grains and grain boundaries in graphene grown by chemical vapour deposition.* Nature Materials, 2011. **10**(6): p. 443-449.

66. Martinez-Galera, A.J., I. Brihuega, and J.M. Gomez-Rodriguez, *Ethylene Irradiation: A New Route to Grow Graphene on Low Reactivity Metals.* Nano Letters, 2011. **11**(9): p. 3576-3580.

67. Vanin, M., et al., *Graphene on metals: A van der Waals density functional study.* Physical Review B, 2010. **81**(8): p. 081408(R).

68. Gong, C., et al., *First-principles study of metal-graphene interfaces.* Journal of Applied Physics, 2010. **108**(12): p. 123711.

69. Giovannetti, G., et al., *Doping graphene with metal contacts.* Physical Review Letters, 2008. **101**(2): p. 026803.

70. Varykhalov, A., et al., *Effect of noble-metal contacts on doping and band gap of graphene.* Physical Review B, 2010. **82**(12): p. 121101(R).

71. Walter, A.L., et al., *Effective screening and the plasmaron bands in graphene.* Physical Review B, 2011. **84**(8): p. 085410.

72. Enderlein, C., et al., *The formation of an energy gap in graphene on ruthenium by controlling the interface.* New Journal of Physics, 2010. **12**: p. 033014.

73. Chuang, F.C., et al., *Electronic structures of an epitaxial graphene monolayer on SiC(0001) after gold intercalation: a first-principles study.* Nanotechnology, 2011. **22**(27): p. 275704.

74. Klusek, Z., et al., *Graphene on gold: Electron density of states studies by scanning tunneling spectroscopy.* Applied Physics Letters, 2009. **95**(11): p. 113114.

75. Shikin, A.M., V.K. Adamchuk, and K.H. Rieder, *Formation of quasi-free graphene on the Ni(111) surface with intercalated Cu, Ag, and Au layers.* Physics of the Solid State, 2009. **51**(11): p. 2390-2400.

76. Wang, B., et al., *Chemical origin of a graphene moire overlayer on Ru(0001).* Physical Chemistry Chemical Physics, 2008. **10**(24): p. 3530-3534.

77. Zhao, L., et al., *Influence of copper crystal surface on the CVD growth of large area monolayer graphene.* Solid State Communications, 2011. **151**(7): p. 509-513.

78. Cho, J., et al., *Atomic-Scale Investigation of Graphene Grown on Cu Foil and the Effects of Thermal Annealing.* Acs Nano, 2011. **5**(5): p. 3607-3613.

79. Rasool, H.I., et al., *Continuity of Graphene on Polycrystalline Copper.* Nano Letters, 2011. **11**(1): p. 251-256.

80. Sandy, A.R., et al., *Structure and Phases of the Au(111) Surface - X-ray-scattering Measurements.* Physical Review B, 1991. **43**(6): p. 4667-4687.

81. Frank, F.C. and J.H. Vandermerwe, *One-Dimensional Dislocations .1. Static Theory.* Proceedings of the Royal Society of London Series a-Mathematical and Physical Sciences, 1949. **198**(1053): p. 205-216.

82. Nie, S., et al., *Graphene/Au(111) interaction studied by scanning tunneling microscopy.* Physical Review B, in print, 2012.

83. Jerng, S.K., et al., *Nanocrystalline Graphite Growth on Sapphire by Carbon Molecular Beam Epitaxy.* Journal of Physical Chemistry C, 2011. **115**(11): p. 4491-4494.

84. Moreau, E., et al., *Graphene growth by molecular beam epitaxy using a solid carbon source.* Physica Status Solidi a-Applications and Materials Science, 2010. **207**(2): p. 300-303.

85. Zhou, M., et al., *Direct graphene growth on Co$_3$O$_4$(111) by molecular beam epitaxy.* Journal of Physics-Condensed Matter, 2012. **24**(7): p. 072201.

86. Snyder, J.D. and J.D. Erlebacher, *Electrochemical Measurement of the Surface Alloying Kinetics of Underpotentially Deposited Ag on Au(111).* Langmuir, 2009. **25**(16): p. 9596-9604.

**Appendix A Graphene Growth on Alternative Substrates**

A.1 Graphene Films on Alternative Au Substrates

Graphene was grown on a variety of Au substrates in addition to the previously discussed Au(111) single-crystal. This is because single-crystal Au substrates may prove unsuitable for wide deployment. They are limited in size and require too much expensive material. Two possibilities that might be more suitable were explored here. Thin Au films deposited on freshly cleaved mica and Au foils were used as substrates. Both of these surfaces were used as substrates for C deposition

Gold films on mica have long been used as templates for surface science studies, particularly by STM. Mica is a phyllosilicate mineral, $K_2O \cdot Al_2O_3 \cdot SiO_2$, which has a monoclinic crystal structure. This structure has very weak interlayer bonding, which is manifested in the near perfect cleavage behavior of mica. Cleaving mica involves carefully delaminating neighboring crystalline layers. The resulting surfaces are atomically smooth over macroscopic areas. After annealing, Au films on freshly cleaved mica possess exceptional surface quality. These often exceed the surface quality of even single-crystal Au.

Gold films were deposited on freshly cleaved mica by electron beam evaporation. Film thicknesses ranging from 100 nm to 250 nm were tested. After annealing, AFM shows the expected outstanding surface quality (**Figure A.1.a**). Typical annealing conditions were 60 minutes at 600 ºC in UHV. AFM also shows pronounced three-fold symmetric surface features. These are easily identifiable in **Figure A.1.a**, and suggest a (111) oriented metal film. C films were subsequently deposited on the Au-mica substrates in UHV as temperatures ranging from 450 ºC to 600 ºC. For these growths elemental C was evaporated from an electron beam heated graphene rod. Example AFM images of films resulting from this procedure are shown in **Figure A.1.b**,**c**.

When C is deposited on Au-mica substrates it first accumulates at Au steps. This is consistent with the observed behavior of elemental C deposited on Au(111) substrates. Further C deposition results in additional growth along Au steps, as well as the development of dendrites growing perpendicular to the step. Branches of C extended as far as ~100 nm from the Au steps. The size of the dendrites is slightly smaller than those observed on Au(111), which is unsurprising due to the lower deposition temperatures. Further characterization of these films was hampered by the Au substrates themselves. Raman spectroscopy did not reveal a detectable C signature. This is likely due to the interaction between Au florescence and the red laser of the Raman system available at the time of these experiments (as opposed to a blue laser, which minimizes Au florescence). As a result, only limited crystallographic information is known about the C deposited on Au-mica substrates.
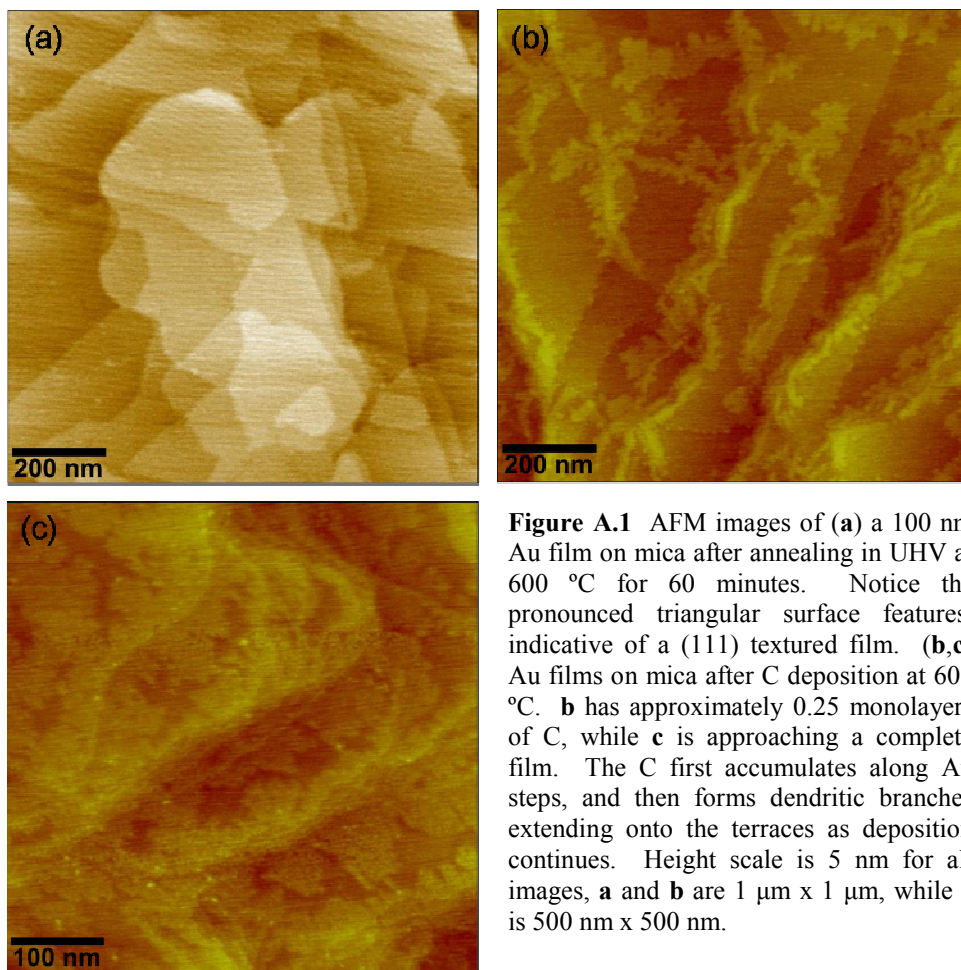
Figure A.1 AFM images of (**a**) a 100 nm Au film on mica after annealing in UHV at 600 ºC for 60 minutes. Notice the pronounced triangular surface features, indicative of a (111) textured film. (**b**,**c**) Au films on mica after C deposition at 600 ºC. **b** has approximately 0.25 monolayers of C, while **c** is approaching a complete film. The C first accumulates along Au steps, and then forms dendritic branches extending onto the terraces as deposition continues. Height scale is 5 nm for all images, **a** and **b** are 1 μm x 1 μm, while **c** is 500 nm x 500 nm.

The utility of Au-mica substrates is severely restricted due to the thermal stability of the mica itself. Above approximately 600 ºC in UHV the mica begins to decompose. This decomposition manifests itself in a dramatic reduction in vacuum, as well as the physical deterioration of the material. Because 600 ºC is insufficient to produce highly ordered graphene films these substrates are unsuitable for graphene growth. A substrate that offers similar surface qualities and higher thermal stability is instead needed.

Gold foils, which are not thermally limited, were also explored as substrates for graphene growth. The 50 μm thick, 99.999% pure Au foils were purchased commercially. Growth was performed in the same manner as on the Au-mica substrates (UHV, elemental C), but at a higher temperature range of 650 ºC to 850 ºC. Preliminary characterization of films grown in this manner is promising. AFM shows a network of ridges in the C film, as shown in **Figure A.2**. These are likely wrinkles formed from thermal stress during sample cooling. This process was described in Section 4.6. Interestingly, the surface of the Au foil is not as smooth as has been observed for Cu foils. This is the case both within individual grains, as well as from grain to grain. The reasons for this are unclear. Further experimentation with surface preparation may allow for substantial improvements in quality. For instance, flame annealing of Au is a well established method for the preparation of high-quality surfaces. Alternative foil
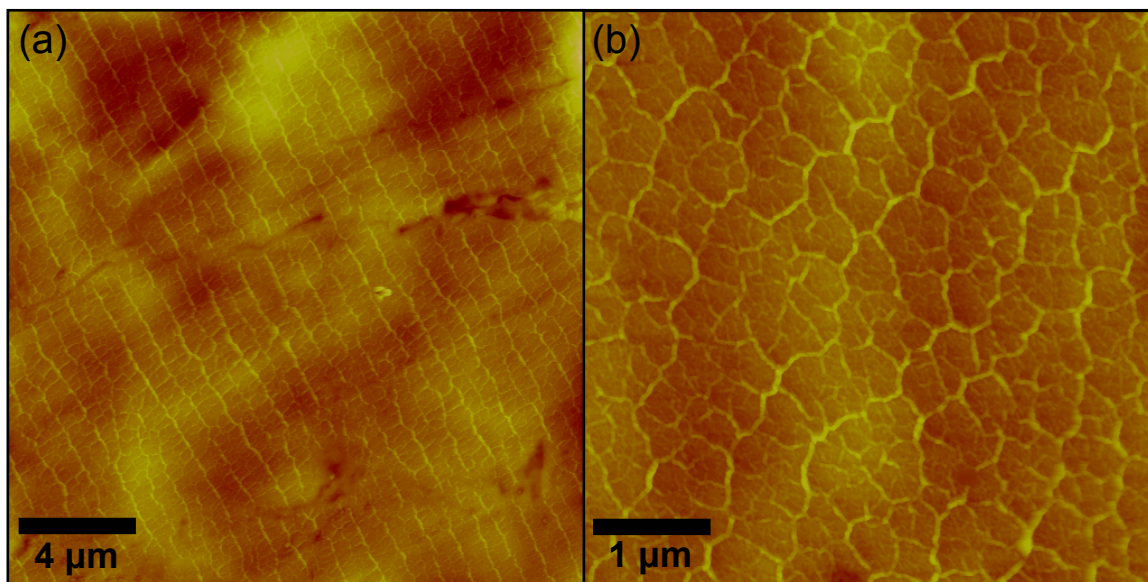
Figure A.2 AFM of graphene films grown on 50 μm thick Au foils by PVD of elemental C in UHV. The matrix of ridges observable in both **a** and **b** are likely wrinkles in the graphene film. Wrinkle formation is driven during sample cooling by the difference in coefficient of thermal expansion between graphene and Au. The extent of the wrinkle matrix suggests a complete, continuous C film (height scales are 200 nm in **a**, and 400 nm in **b**).

processing techniques have also been demonstrated to produce highly (111)-textured Au foils with individual grains millimeters across [86]. More thorough characterization of existing films is also necessary to ascertain their crystalline quality. Raman spectroscopy with an appropriate wavelength laser will yield this structural information. Electronic measurements after transfer to a dielectric substrate are also an important step in evaluating this growth method. Many of the advantages of Au(111) single crystal substrates may be exploited to grow large area graphene films on Au foils.

A.2 Graphene Growth on Ge(111)

Germanium is an interesting candidate as a substrate for graphene growth. Like the other substrates examined here, it has a negligible C solubility. This should allow it to support monolayer graphene growth. Ge wafers are also available with the exceptional surface qualities common to semiconductor technology. The suitability of Ge for integration into a standard CMOS production facility is another intriguing property. This is especially true because carbide formation during C deposition prevents the use of Si as a graphene substrate. Ge also has an extremely low vapor pressure. The resulting static growth surface and reduced roughening are both positive attributes. Finally, Ge offers the opportunity to explore graphene growth on a covalently bonded substrate; something which has previously been restricted to the thermal decomposition of SiC.

To evaluate Ge as a substrate for graphene growth C films were deposited on Ge(111) wafers in UHV. C was evaporated from an electron-beam heated graphite rod,
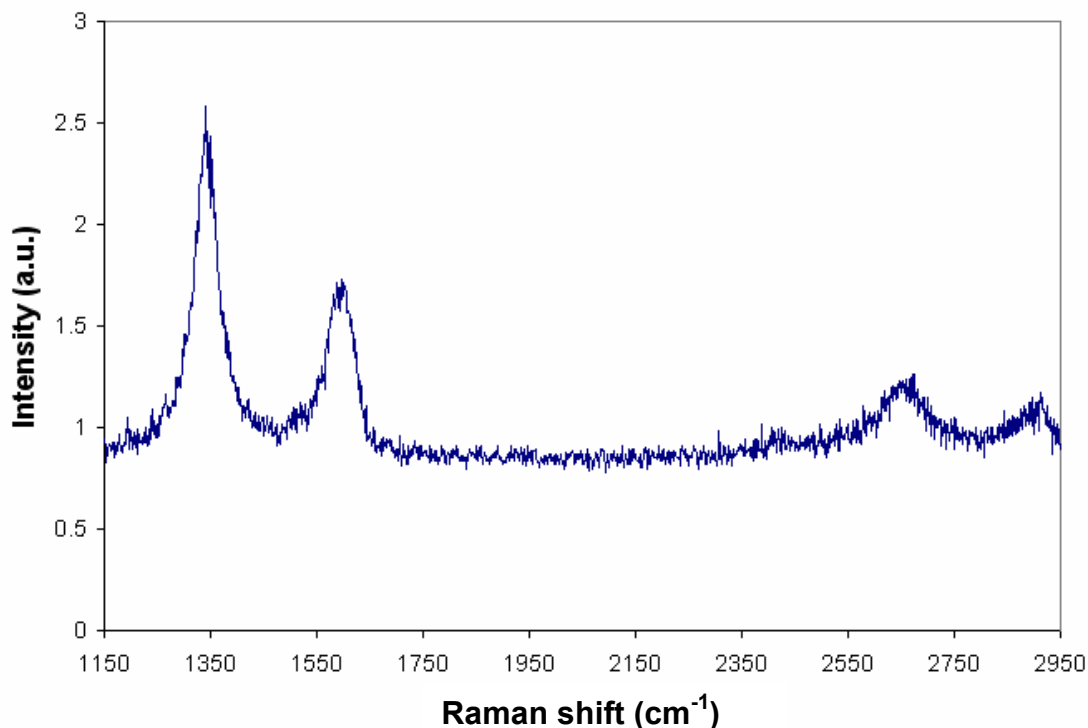
Figure A.3 Raman spectrum of a C film deposited on Ge(111) at 750 °C. The D (~1350 cm^{-1}) and G (~1595 cm^{-1}) characteristic peaks are both clearly visible, as are the second order modes of both. The presence of the second order modes is indicative of a reasonable coherence length in the C crystal. An increase in coherence length corresponds with larger sp^2 bonded domains, and additional long-range crystalline order [52].

and substrate temperatures from 500 °C to 800 °C were used. A representative Raman spectrum for a C film deposited on Ge(111) in this manner and subsequently transferred to a SiO$_2$ support is shown in **Figure A.3**. The D and G peaks of sp^2 bonded C are clearly visible, as are the second order modes of both peaks. The D-to-G peak height ratio exhibited by C films grown on Ge(111) is suggestive of a moderately disordered, sp^2 bonded C film. The crystalline quality falls short of films produced on metals [39], but is superior to results reported for direct C deposition on dielectric substrates [83-85]. Because these results are only preliminary it is possible that significant improvements in film quality may be achieved. For instance, the films evaluated here were deposited in only 60 to 120 seconds. This is a much higher growth rate than is typically used during graphene growth. Slower growth would allow the film more time to develop the desired level of crystalline order.

Perhaps the most intriguing aspect of graphene films deposited on Ge(111) is the ease with which they may be transferred off the growth substrate. The transfer of graphene films from the growth substrate to a dielectric support typically requires both a polymer support layer and the complete dissolution of the initial substrate. This necessitates possibly hazardous chemicals, destroys the growth substrate, and is a generally cumbersome procedure. In contrast, C films grown on Ge(111) may be lifted off using only a warm water bath. This preserves the Ge substrate for use in subsequent

growths. To do so, the graphene-Ge(111) samples are first soaked in water at ~60 ºC for 15 minutes. The wafer is then gently lifted from the water and slowly lowered back in while held at and angle to the surface. The graphene film lifts off the Ge substrate during reinsertion into the bath. Either the surface tension of the water or the buoyancy of the C film is sufficient to delaminate it. At this point the C film floats on the surface of the water until it is captured by bringing a new support up from underneath it. An optical image of a graphene film grown on Ge(111) and transferred to a SiO$_2$ support using this procedure is shown in **Figure A.4**.

The reason graphene films grown on Ge(111) may be lifted off with only water has yet to be conclusively identified. However, it is possible to offer informed speculation. Unlike Cu, the oxide of Ge is soluble in water. It is possible that a continuous oxide layer develops at the Ge-graphene interface while the sample is soaking in water. This oxide layer may then progressively dissolve as the sample is slowly lowered back into the water bath, releasing the C film in the process. The ease of transfer of C films grown on Ge combined with the ability to reuse the substrates makes this an attractive way to grow graphene. This synthesis method offers many potential advantages if improvements in graphene crystalline quality are realized.
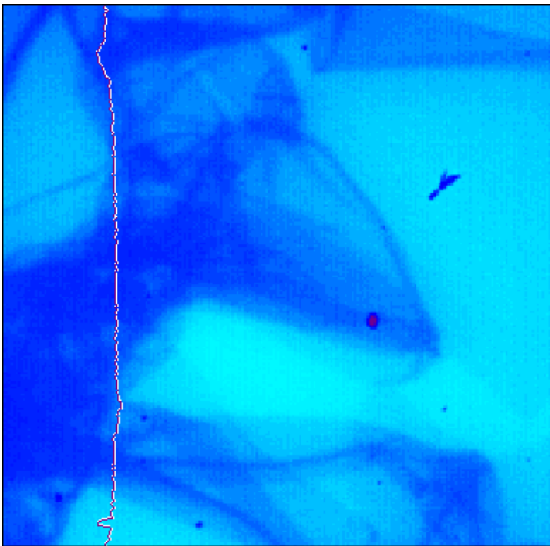
Figure A.4 An optical image of a C film, deposited on Ge(111) at 750 ºC, and subsequently transferred to an SiO$_2$ support. The graphene is the darker regions of the image. The transfer process of C films off Ge substrates does not require dissolving the Ge, or the use of a polymer support. This particular film became folded onto itself during transfer, showing the delicate nature of the process.

Appendix B Numerical predictions of the C adatom gas concentration

Surface diffusion of C plays an integral role in graphene growth on Cu(111). It influences both the nucleation and growth behavior. This is because C concentration gradients develop, leading to an inhomogeneous distribution of adatoms on the substrate surface. To better understand the relationship between surface diffusion and graphene growth it is useful to numerically estimate the spatial distribution of the C concentration. This is particularly true because the specific geometry of the sample surface may be used to set the boundary conditions for the calculations. The resulting concentration maps allow for direct comparison with the observed nucleation and growth behavior of graphene on Cu(111), as was done in **Figure 4.1** and **Figure 4.11**.

Generating a concentration map requires numerically estimating a solution for the diffusion equation for a given surface configuration. The diffusion equation, which is a partial differential equation, takes the form:

$$\partial\varphi(\mathbf{r},t)/\partial t = \nabla\cdot[D(\varphi,\mathbf{r})\nabla\,\varphi(\mathbf{r},t)]$$

where $\varphi(\mathbf{r},t)$ is the concentration of the diffusing material (C in this case), $\mathbf{r}$ is the position, t is time, and $D(\varphi,\mathbf{r})$ is the diffusion coefficient for density φ at position $\mathbf{r}$. In this case a number of simplifying assumptions were made. Implicit in this model is the assumption that graphene growth occurs slowly relative to surface diffusion. Thus, the adatom gas maintains a steady-state throughout growth. The diffusion coefficient, D, was treated as independent of concentration and position, making it a constant. The flux experienced by the surface from the C vapor was assumed to be uniform over the sample and constant it time. Finally, because the C is confined to the surface of the substrate we only need to consider two dimensions. When these assumptions are applied to the diffusion equation it simplifies to:

$$\partial\varphi/\partial t = D(\partial^2\varphi/\partial\mathbf{x}^2 + \partial^2\varphi/\partial\mathbf{y}^2) + f$$

where D is now the scalar diffusivity, $\mathbf{x}$ and $\mathbf{y}$ denote the position on the sample surface, and f is the flux of C atoms from the vapor to the surface. This equation allows us to estimate the distribution of C adatoms on the substrate surface.

The specific geometry observed for the substrate surface was used to establish the boundary conditions of the diffusion equation. To do so the perimeter of the field of view was treated as a perfect mirror (net flux = 0). Furthermore, each existing graphene island was modeled as a perfect sink ([C] = 0 within the island). A mesh could then be fitted to the surface configuration, with a higher mesh density near fine surface features. This surface mesh produced the discrete elements needed to numerically solve the diffusion equation. The diffusion equation was iteratively solved for the given mesh, with the boundary conditions enforced, until an approximate steady state was reached ($\partial\varphi/\partial t \approx 0$ for all $\mathbf{x},\mathbf{y}$). The resulting distribution of concentrations, $\varphi(\mathbf{x},\mathbf{y})$, could then be compared with experimental observations.

The concentration maps generated through this procedure were correlated with two different aspects of graphene growth on Cu(111). Graphical depictions of the C surface concentration were generated using a gray-scale, with regions of high concentration shaded lighter. These were compared with the locations of secondary graphene island nucleation (**Figure 4.1**). The strong correlation between the two shows that unlike primary nucleation, which is instigated by surface inhomogeneities, secondary nucleation is mainly the result of a locally high C adatom concentration. Additionally, estimates for the graphene growth rate could be generated by inspecting the C flux experienced by each perimeter section of existing islands, as was done in **Figure 4.11**. The flux from each mesh element bordering a sink (or graphene island) yields this quantity, pointing to the importance of using a fine mesh around the perimeter of existing islands. The excellent agreement between the estimated fluxes and the observed growth rate of graphene islands on Cu(111) demonstrates the governing influence of surface diffusion.